# Exploring Vascular Roots of BOLD: A New Approach to fMRI Modelling

**Parineeta Ekhande**

Student Number: 14295083

**Supervisor: Dr. Steven Miletic**

**Literature Thesis**

**Master in Brain and Cognitive Sciences**

**Abstract:**

Functional Magnetic Resonance Imaging (fMRI) has emerged as a key tool for mapping brain activity by using the Blood Oxygen Level Dependent (BOLD) signal, which indirectly reflects neural activity through changes in cerebral blood flow and oxygenation. However, the BOLD signal's accuracy is inherently limited by the complex and variable architecture of cerebral vasculature, raising questions about its spatial and temporal resolution. Thus, in this thesis we explore integration of cerebrovascular anatomy into BOLD modelling. We present a review of literature on anatomy of cerebral vasculature, non-invasive structural MRI techniques such as Magnetic Resonance Angiography (MRA) and Magnetic Resonance Venography (MRV) for mapping brain vasculature and explore their functional means (fMRA and fMRV) as a potential technique for tracking the roots of neural activity.

UNIVERSITY
OF AMSTERDAM

## Introduction

The working of a human brain has held interests of scientists and laymen alike for centuries. Knowledge about the brain was limited for the longest time, being gained primarily through studying animal brains, diseased brains, or brain samples. One thing in common between all the old techniques was that their studies could only be conducted on post-mortem brains, it was impossible to conduct non-invasive studies on live human brains due to lack of methods. Following the development of medical equipment, non-invasive technologies such as EEG, MEG gave information about the temporal aspects of brain activity (Bollman & Barth, 2021). The development of Magnetic Resonance Imaging (MRI) facilitated the gain of spatial information. MRI has proved to be an unparalleled diagnostic method due to its ability to differentiate between magnetic susceptibility of various tissues to produce structural images of organs including the central nervous system (Logothetis, 2008). For neuroscientists, the ability of MRI to be able to distinguish between oxygenated and de-oxygenated blood becomes of paramount as we exploit this to understand the neural mechanisms of the brain (Logothetis & Wandell, 2003). Development of fMRI (functional Magnetic Resonance Imaging) to measure these haemodynamic changes due to neural activity and draw conclusions about neural mechanisms and cognitive capacities (Logothetis, 2008).

As explained in (Logothetis & Wandell, 2003) & (Logothetis, 2008), BOLD i.e. blood oxygen level-dependent contrast is one of the most widespread non-invasive contrasts. In the brain, the extent of local field inhomogeneities is influenced by the physiological state and the composition of the local blood supply coming from the local vascular anatomy, which is linked to neural activity. Therefore, T2* measurement indirectly reflects neural activity and can be measures at high resolution across the brain. The BOLD contrast is influenced by neural activity-induced changes in the concentration of oxygenated versus deoxygenated blood. Deoxyhaemoglobin (dHb), which is paramagnetic, affects the MR signal differently from oxygenated haemoglobin (Hb). The shortcoming of fMRI is that the signal's temporal and spatial aspects are a subject to physiological and biological constraints and only indicate mass neuronal activity (Logothetis, 2008). An area of the brain that is largely active receives blood from the surrounding vessels. This change in oxygenation captured by fMRI is processed using statistical analysis and modelling to pinpoint the area of activity. However, that signal comes from a general mass of brain and not a specific position in the brain giving rise to the question, where exactly does the BOLD signal originate from and how can we accurately measure it?

One idea to explore these questions is by integrating the information about the cerebrovascular physiology, especially the differences in blood absorption, volume and velocity in the arteries, veins and capillary structures. We can integrate this information into BOLD modelling by combining conventional functional imaging with specialised sequences that can map the vasculature and measure these differences (such as MRA and MRV). Conventional BOLD modelling does not consider the cerebrovascular anatomy. There have been recent studies that have tried to bridge this gap such as Vascular Anatomy Network model (Gagnon et al. 2015; Gagnon et al. 2016), however the attempt is limited to rodent brains and not human brains. To this avail, we review the literature regarding different ways that we can map the vasculature and integrate the information into BOLD modelling. We start by revisiting fMRI basics, then move onto detailed explanation of the cerebrovascular anatomy followed by two non-invasive MRI techniques that we believe have the potential for integrating into BOLD modelling algorithms.

## BOLD Overview

Neuronal activity either provoked by a spontaneous or is stimulus-provoked causes changes in blood flow and oxygenation in different vascular structures such as the arteries, veins and capillaries which is detected by functional MRI (Uludag et al. 2009). fMRI is sensitive to cerebral blood volume, changes in oxygenation and deoxygenated of haemoglobin and cerebral blood flow due to neuronal activity. There are multiple parameters that affect the spatial and temporal properties of the fMRI signal such as vascular anatomy, magnetic field strength, echo time (TE), repetition time (TR), RF pulses, gradient coils (Uludag & Blinder, 2017), acquisition strategies and sequences types (GE, SE, ASL,VASO etc). The same neuronal activity, related change in CBV, CBF and oxygenation the fMRI signal varies for different imaging parameters (Logothetis, 2008) making it an indirect measure of neural activity, its characteristics defined by vascular anatomy and MRI parameters.

According to the review by Uludag & Blinder, 2017, fMRI at 7T using gradient-echo (GE) or spin-echo (SE) sequences has shown improved statistical power and sensitivity for detecting neuronal activity compared to lower field strengths like 1.5T and 3T. High-resolution fMRI studies aim to investigate fine-scale cortical structures like columns and layers. At this level of detail, understanding the organization of the brain's vasculature, as well as the control of blood flow changes and associated oxygenation and blood volume changes, and their relationship to neuronal structures, becomes crucial. Additionally, the time course of the fMRI hemodynamic response is dependent on the magnetic field strength used.

Thus, to understand the origins of neural activity, it is essential to understand the mechanism of fMRI and vascular anatomy. The reason for further focus on vascular properties is due to the direct role it plays in describing field strength dependence on fMRI signal.

## Basics of fMRI Signal Generation

fMRI measures changes in blood oxygenation and flow that occur due to neural activity. When neurons become active, they consume oxygen, increasing the local concentration of deoxygenated haemoglobin (dHb). The paramagnetic dHb creates magnetic field distortions around blood vessels, affecting the T2* relaxation time used to generate the fMRI signal. The hemodynamic response describes how neural activity leads to changes in blood flow, volume, and oxygenation. Increased brain activity dilates blood vessels and increases oxygen-rich blood flow, reducing dHb and increasing oxygenated haemoglobin. This neurovascular coupling indirectly relates the fMRI signal to neural activity, with the hemodynamic response function modelling the expected BOLD signal.

Typically, a fMRI signal acquisition would consist of RF excitation of hydrogen protons and signal detection after a delay (echo time (TE)). Hydrogen atoms start spinning in the magnetic field and when flipped by the RF pulse they circle back to its original state. Thus, moving a magnet which is the human through a receiver coil produces signal - **the MRI Signal** or when the signal is related to relaxation of deoxygenated blood – **the fMRI signal.**

The MRI signal decays over time, and this decay can be described by an exponential function $(exp(-TE/T2*))$ with a relaxation time constant called T2*. This type of MRI sequence is called Gradient Echo. The signal decay happens faster when the magnetic field is more uneven within the measurement area. Applying a 180-degree RF pulse at a certain time can refocus some of the signal loss, resulting in a different MRI sequence called Spin Echo with a relaxation time constant called T2. Deoxygenated haemoglobin and oxygenated haemoglobin have different magnetic properties, so changes in blood oxygenation can alter the magnetic susceptibility of the tissue, affecting both the T2* and T2 values (Uludag & Blinder, 2017). CBV, CBF, and cerebral metabolic rate of oxygen (CMRO$_2$) contribute to blood oxygenation change (Buxton et al. 2004). As explained above, the BOLD signal is influenced by neural activity-induced changes in the concentration of oxygenated versus deoxygenated blood resulting in magnetic field inhomogeneities in and around the blood vessels affecting the MRI signal.

The single exponential decay does not fully describe the experimentally detected fMRI signal due to several factors explained in the review by Uludag & Blinder, 2017. Thus, the basic equation for quantifying fMRI signal for both SE and GE fMRI is given by Uludag et al. 2009 –

$$S_{tot} = (1 - CBV) . S_{ex} + \sum_i \emptyset_i . S_{in,i} . CBV_i$$

Wherein $S_{tot}$, for both GE and SE MRI sequences includes the intra- and extra-vascular contributions ($S_{in,i}$ with $i$ denoting the different vascular compartments and $S_{ex}$, respectively), weighted by their corresponding volumes ($CBV_i$) and $(1 - CBV)$, respectively. The term $\emptyset$ is the relative proton spin density between intra and extravascular spaces whose value is close to 1 due to high permeability of capillaries to water (Uludag et al. 2009; Uludag & Blinder, 2017; Liu et al. 2003). This term is also used to describe the apparent spin density by incorporating inflow effects or spin tagging Arterial Spin Labelling (ASL) fMRI for measuring CBF (Buxton et al. 2004) or spin inversion for Vascular Space Occupancy (VASO) fMRI for measing CBV (Lu et al. 2003). Further substituting these parameters into the equation and calculating signal changes allows to predict fMRI signal as a function of field strength, oxygenation and CBV (Uludag & Blinder, 2017). The Uludag et al. 2009 study conducted by the same investigators found that GE fMRI is dominated by macro-vasculature and SE fMRI had high tissue specificity for all field strengths they had considered.

In terms of advancing BOLD modelling simulations for understanding blood flow changes and their impact on the fMRI signal, previous studies on extra-vascular relaxation rate simulations, such as those by Boxerman et al. (1995a&b) and Ogawa et al. (1993), employed a single cylinder model to representing a blood vessel to model these changes. More recently, Gagnon and colleagues advanced this method by utilizing an in vivo realistic vascular network model (VAN) acquired through two-photon microscopy (Gagnon et al., 2015). Their model accurately reflected the vascular architecture, cerebral blood volume (CBV) fractions, CBV and cerebral blood flow (CBF) changes, and blood oxygenation observed in the rat cortex. This research confirmed earlier findings that SE fMRI has higher spatial specificity than GE fMRI at high magnetic field strengths while also introducing the discovery that the GE fMRI signal is influenced by the tissue's orientation relative to the magnetic field (Uludag & Blinder, 2017).

Numerical simulations on extra-vascular relaxation times typically assume mono-exponential signal decay within a grey matter environment with a specific relaxation time (Uludag & Blinder, 2017). Pflugfelder et al. (2011) assessed the impact of these assumptions using both a random network of cylinders (mimicking microvasculature) and a single cylinder model (representing macro-vasculature) for SE fMRI, as GE fMRI is predominantly influenced by macro-vasculature.

They found that including a second compartment (e.g., CSF) in simulations decreased microvascular specificity due to increased weighting toward surface veins.

Uludag & Blinder, 2017 observed in their review that one aspect these studies do not extensively consider is the varying oxygenation along blood vessels, especially in capillaries where oxygenation can drop significantly under normal physiology. Gagnon et al. (2015) in their VAN model incorporated this variability into their models, highlighting its influence on magnetic field inhomogeneities and subsequent signal decay. These effects however are expected to have a small impact on the overall fMRI signal coming from the arteries and veins due to homogenous distribution of oxygen (Uludag & Blinder, 2017).

Overall, while certain factors such as CSF inclusion suggest reduced microvascular specificity for SE fMRI, other elements like non-monoexponential decay and oxygenation inhomogeneity predict increased microvascular signal contribution (Uludag & Blinder, 2017). Furthermore, susceptibility effects from neighbouring voxels also influence signal decay, particularly affecting GE fMRI in the upper cortical layers (Uludag & Blinder, 2017). At ultra-high field strengths, expected to be devoid of extra-vascular signals from draining veins, SE-fMRI might offer highly specific functional signals optimal for neuroimaging, despite technical limitations like RF energy deposition (such as SAR effect) and transmit field inhomogeneities (Uludag et al. 2009). Understanding fMRI spatial specificity and temporal characteristics requires careful consideration of MRI parameters and vascular physiology, specifically baseline and stimulus-induced blood oxygenation and CBV. Given the crucial role that vascular architecture plays in modulating these fMRI signals, a deeper understanding of the brain's cerebrovascular structure is essential.

**Cerebrovascular Architecture**

The cerebral vasculature, a vital system for supplying blood to the brain, is intricate and highly variable across human brains. It comprises the anterior and posterior circulations, linked through the circle of Willis. The arterial system, with its key junctions in the anterior and posterior circulation, constitutes the primary sources of arterial blood circulation. Specifically, the anterior circulation originates from the internal carotid arteries, while the posterior circulation stems from the vertebral arteries (Chandra et al. 2017).

Like all circulation in the human body, the blood flow to the brain originates from the heart. Oxygenated blood is ejected from the left ventricle into the aorta during systole (Chandra et al. 2017). From the aorta, which ascends to the aortic arch, three main branches emerge (Drake et al. 2015). These branches include the left common carotid artery and the vertebral arteries, originating from the subclavian arteries on either side of the body (Drake et al. 2015; Standring, 2015).

The common carotid and vertebral arteries constitute the anterior and posterior cerebral circulation, respectively, serving as the primary blood supply routes to the brain (Chandra et al. 2017). Moving up to the Circle of Willis, we dive further in detail into the anterior and posterior circulations.

However, one thing that is relevant for neuroscientists that are part of the fMRI community is that the most relevant vascular information is the one that relates post capillary oxygenation and blood volume changes (Uludag & Blinder, 2017). However, for the sake of providing a complete overview of the vascular anatomy, we discuss the entire supply and drainage system known, mapped and reviewed till date along with the information regarding which structures supply & drain blood to which parts of the brain.
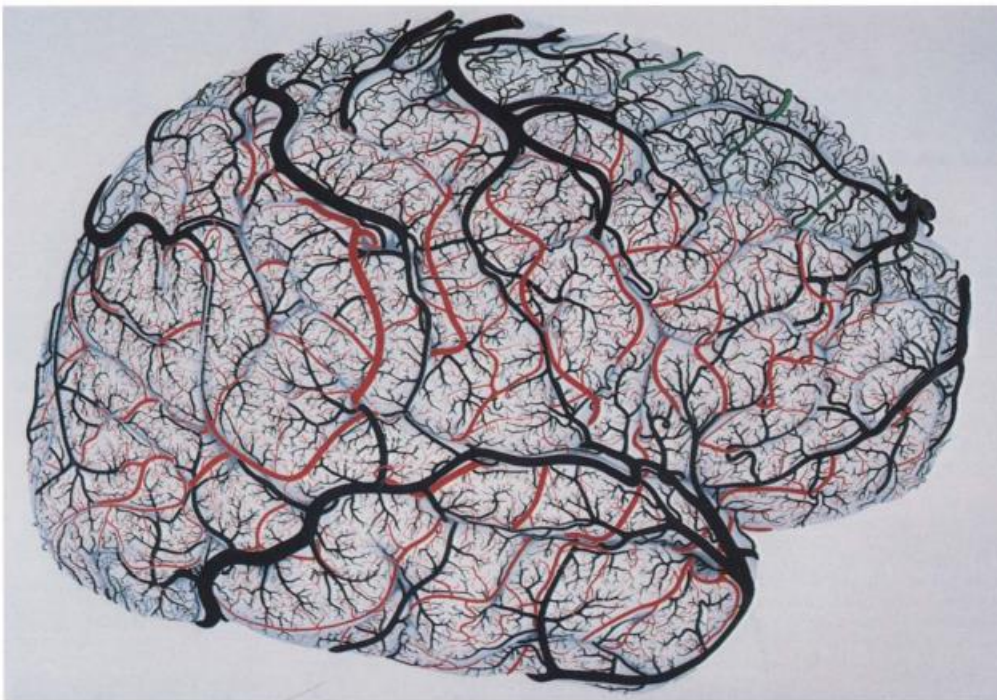


Fig. 1. Drawing of the cortical pial vessels from Duvernoy et al. 1981 (Fig. 1.) showing branches of middle cerebral artery (red), anterior cerebral artery (green) & posterior cerebral artery (blue)

**The Anterior Circulation:**

The anterior circulation provides circulation to a large portion of the forebrain, including frontal, temporal and parietal lobes as well as diencephalon and internal capsule (Chandra et al. 2017). Anterior circulation amounts to 72% of cerebral flow as measured by phase-contrast MRI (Zarrinkoob et al. 2015). Thus, the first stop in the anterior circulation is the Anterior Cerebral Artery.

The ACA provides blood to the most medial part for the cortical surface located along the longitudinal fissure including areas of the frontal lobe and superior medial parietal lobe (Chandra et al. 2017). The route of the ACA arises from the anterior clinoid portion of ICA towards the longitudinal fissure. At the fissure it forms an anastomosis that is called the anterior communicating artery (Chandra et al. 2017). The anterior communicating artery is the first major stop along the ACA route (could also be re-termed as the first segment of the rest of the 5). ACA provides blood to deep cortical structures.

The ACA is divided into several segments, each with specific boundaries, branches, and regions supplied, as well as notable anatomical variants. The A1 segment, situated between the internal carotid artery (ICA) and the anterior communicating artery (ACoA) (Chandra et al. 2017).

It branches into the medial lenticulostriate artery, ACoA, and small perforating arteries, supplying the caudate nucleus, anterior limb of the internal capsule, and other regions (De Freitas et al. 2009). The A2 segment extends from the ACoA to the bifurcation forming the pericallosal and supramarginal arteries (Chandra et al 2017). It branches to the recurrent artery of Heubner (Stefani et al. 2000) and orbitofrontal artery, supplying the anterior caudate nucleus, internal capsule, and frontal lobe (Standring, 2015). The A3 segment, also known as the pericallosal artery, runs around the genu of the corpus callosum and supplies blood to the corpus callosum, superior frontal gyrus, and medial hemisphere (Harrigan & Deveikis, 2012). The A4 and A5 segments consist of smaller branches over the corpus callosum (Medcalf et al. 2016; Manbachi et al. 2011; Gupta et al. 2016; Li et al 2017).

Along the ICA, the next stop of consideration is the Anterior Choroidal Artery (AChA). Its a branch of ICA that arises from the supraclinoidal portion (Palomeras et al., 2008) but is also found to arise from either the MCA (Middle Cerebral Artery) or PCoA (Rhoton et al. 1979; Herman et al. 1966). The deep branches of AChA supply blood to the posterior two-thirds of the internal capsule, nearby optic and auditory pathways, medial part of the globus pallidus, and tail of the caudate nucleus.

The superficial branches cover areas such as piriform cortex and uncus, hippocampal head, amygdala, and most lateral part of the thalamic lateral geniculate nucleus. (Feekes et al. 2005; Ghika, 1990; Hamoir et al. 2004; Palomeras et al. 2008; Tatu et al. 1998).

**Middle Cerebral Artery**

The MCA is one of the largest and complexly distributed cerebral vessels which has found to have a relatively consistent route throughout individuals (Chandra et al. 2017). The MCA arises from the ICA and travels laterally along the ventral surface of the frontal lobe before entering the Sylvian fissure, which separates the temporal lobe from the insular cortex (Standring 2015; Rhoton et al. 1979; Chandra et al. 2017). In this area, the artery usually divides into two or three main branches. These branches then extend upwards and downwards over the insular surface, providing blood supply to most of the lateral surface of the cerebral hemisphere. This includes areas such as insular cortex, opercular surface, superior and middle temporal gyri, inferior parietal lobule along with a significant portion of postcentral gyrus in the parietal territory; and inferior and middle frontal gyri, much of precentral gyrus, and lateral part of orbital surface in the frontal territory (Chandra et al. 2017).

The middle cerebral artery (MCA) is divided into several segments, each with distinct anatomical paths, branches, and areas supplied. The M1 segment, also known as the horizontal segment, originates at the carotid bifurcation, transitions into the middle cerebral artery, and extends superiorly into the region between the temporal lobe and the insula. It branches into the medial and lateral lenticulostriate arteries and the anterior temporal artery. This segment supplies blood to the head and body of the caudate nucleus, the upper part of the anterior limb, the genu, the anterior portion of the posterior limb of the internal capsule, the putamen, the lateral pallidum, and the anterior temporal lobe. (Chandra et al. 2017; Standring, 2015; Ferro et al. 2014; Villringer & Einhäupl, 1997). The M2 segment, or insular segment, enters at the temporal lobe and insula, ascending along the insular cleft before making a hairpin turn at the insular sulcus. It branches into 2-3 main trunks, which are divided into superior and inferior divisions. The superior division includes the orbitofrontal artery, prefrontal artery, precentral artery, and central arteries, supplying the orbitofrontal area to the posterior parietal lobe. The inferior division consists of the temporopolar artery, temporo-occipital artery, angular artery, and anterior, middle, and posterior temporal arteries, supplying the temporal pole to the angular area of the parietal lobe (Chandra et al. 2017; Standring, 2015; Ferro et al. 2014; Villringer & Einhäupl, 1997). The M3 segment, known as the opercular segment, starts at the apex of the hairpin turn in the insular sulcus and extends to the lateral convexity of the cerebral hemisphere.

Its terminal branches form 2-3 main trunks that supply the frontal, parietal, and temporal operculae (Chandra et al. 2017; Standring, 2015; Ferro et al. 2014; Villringer & Einhäupl, 1997). The M4 segment, or cortical segment, begins at the surface of the Sylvian fissure, spreading over the cerebral hemisphere and arising between the frontal, parietal, and temporal lobes (Standring 2015; Carpenter et al. 1954). It gives rise to cortical branches that supply the hemispheric surface of the frontal and parietal lobes (Bradley, 2004).

### The Posterior Circulation

Also known as the 'vertebrobasilar circulation' posterior circulation provides blood about a one-third of the total flow perfusing the brain (Chandra et al. .2017). It consists of the vertebral arteries, the basilar artery created by the fusion of the vertebrals, and various branches supplying blood to different parts of the brain. This circulation mainly supplies blood to the posterior portion of the brain including occipital lobe, most parts of brainstem, and all of cerebellum. (Standring et al. 2015; Hussein et al. 1988). We will now delve into the organised overview of the branches starting with the vertebral arteries.

### Vertebral Arteries

Vertebral arteries are divided into four segments for simplification. They are paired and bilateral arteries that originate from the subclavian vessels on each side of the body. The first three segments of the vertebral arteries are extracranial (Chandra et al. 2017).

The first segment, V1, extends from the subclavian origin to the vertebral transverse foramen and is commonly affected by vertebral artery infarction (Solberg & Eggen, 1971). Following V1, the V2 segment passes through the transverse foramen. The subsequent V3 segment loops around the atlas and enters the dura before transitioning into V4 -the intracranial segment of the vertebral arteries that runs from its dural entrance to either rostral medulla or caudal pons. This section has various vascular responsibilities including giving rise to important branches like posterior inferior cerebellar artery (PICA) (Hussein et al. 1988) and contributing small branches proximal to the anastomosis with contralateral counterpart forming descending anterior spinal artery.

**Posterior Inferior Cerebellar Artery**

PICA is the largest branch of the vertebral artery that provides arterial blood to the dorsolateral region of medulla, inferior cerebellar peduncle to reach the ventral surface of the cerebellum (Chandra et al. 2017; Hussein et al. 1988; Standring et al. 2005).

**Anterior Spinal Artery**

The artery runs along the anterior median fissure down the entire length of the spinal cord while also providing blood to part of anterior medulla that the artery rests upon (Chandra et al. 2017)

**Basilar Artery**

The basilar artery is a major blood vessel in the posterior circulation of the cerebral circulation. It is formed by the fusion of the two vertebral arteries at the base of the skull. The basilar artery supplies blood to critical structures in the brainstem, including the pons, medulla, and cerebellum. It gives off several branches, including the anterior inferior cerebellar artery (AICA), superior cerebellar artery (SCA), and posterior cerebral artery (PCA) (Chandra et al. 2017; Hamoir et al. 2004; Hussein et al. 1988). The AICA supplies the anterior and inferior aspects of the cerebellum, while the SCA supplies the superior aspect of the cerebellum (Chandra et al. 2017; Hamoir et al. 2004; Hussein et al. 1988; Standring et al. 2005). The PCA supplies the occipital lobe and parts of the temporal and parietal lobes (Chandra et al. 2017). Understanding the anatomy and function of the basilar artery is crucial for diagnosing and treating cerebrovascular diseases in the posterior circulation. The basilar artery is a major branch of the vertebral arteries and plays a crucial role in the posterior cerebral circulation. It is formed by the fusion of the two vertebral arteries at the level of the pons (Chandra et al. 2017). The basilar artery supplies blood to critical structures in the brainstem, including the brainstem autonomic centres. It also gives rise to important branches that supply the cerebellum, posterior cerebral cortex, and other structures in the posterior circulation (Chandra et al. 2017).

**Venous Circulation**

Cerebral blood after passing through the arteries proceeds to the capillary beds, undergoes metabolic modifications wherein O2 and nutrients are stripped from the arterial blood and loaded with CO2 and metabolites, enters the venous system. The cerebral venous anatomy is characterized by significant variability, differing not only among individuals but also between hemispheres within a single brain, complicating classification. Nonetheless, some general patterns exist, essential for understanding the anatomy (Chandra et al. 2017).

The cerebral venous system comprises two primary networks based on their cortical positions: the superficial dural venous sinuses and the deeper cerebral veins (Bell et al. 2009). These sinuses are typically formed between the periosteal and meningeal layers of the dura mater and are located near the cranial bones.

A significant component, the confluence of sinuses (CS), acts as a collection point for venous blood from several sinuses, including the superior sagittal sinus, straight sinus, occipital sinus, and transverse sinuses, which connect to the jugular bulb via the sigmoid sinuses (Tatu et al. 2009). The inferior sagittal sinus, unlike other sinuses formed by both meningeal and periosteal dura, runs along the free edge of the cerebral falx and continues as the straight sinus to join the CS (Chandra et al. 2017). The bilateral cavernous sinuses positioned superior to the sphenoid bone and bordered by the superior orbital fissure, temporal bone, and sella turcica, receive blood from various veins including the superior and inferior ophthalmic veins and the superficial middle cerebral veins. These sinuses are connected across the midline by intercavernous sinuses and drain into the jugular vein through the superior and inferior petrosal sinuses (Yasuda et al. 2008; Tatu et al. 2009). Additionally, the sigmoid sinus, a continuation of the transverse sinus, directs blood to the internal jugular vein (Tatu et al. 2009).

Communication between the dural sinuses and extracranial veins occurs via emissary veins, which facilitate blood flow between the face, scalp, and brain, and through the vertebral venous plexus, which receives blood from the inferior petrosal and occipital sinuses (Schaller, 2004; Tatu et al. 2009; Kawamata et al. 2001).

The cerebral veins, responsible for draining the brain's parenchyma, are classified into superficial and deep veins. Superficial veins, running along cortical sulci, drain the brain's cortex and include named veins like the superficial middle cerebral veins and the superior and inferior anastomotic veins. Deep cerebral veins, which drain the deep white and grey matter structures, converge centrally at the great cerebral vein of Galen. Notable deep veins include the internal cerebral veins, the basal veins of Rosenthal, and the great cerebral vein of Galen. These veins collectively drain blood from various brain regions and direct it towards the straight sinus (Schaller, 2004; Chandra et al. 2017).

In conclusion, the cerebral venous system, with its complex and variable anatomy, plays a crucial role in draining blood from the brain. The dural venous sinuses and cerebral veins, through their intricate networks and numerous anastomoses, ensure efficient blood flow and significant compensatory capacity.

This understanding of the cerebrovascular anatomy is vital for diagnosing and treating conditions such as cerebral venous thrombosis and brain tumours but also to understand the underlying vascular anatomy of the brain areas imaged during neural activity. Having now detailed the cerebrovascular anatomy, we will transition to the imaging techniques used to visualize the vasculature.
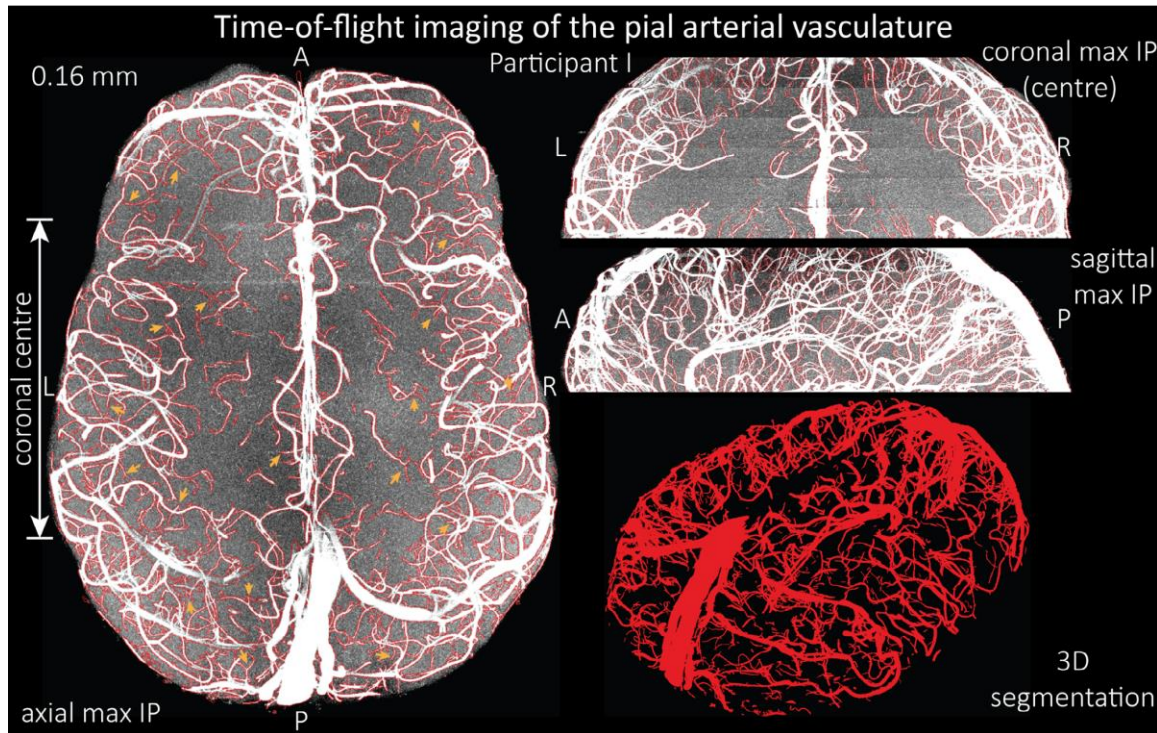


Fig. 2. From Bollman et al. 2021 (Fig. 6) showing TOF – MRA at 7T image of pial arterial vasculature. Right: Coronal maximum intensity projection and segmentation of the central part of the brain (top), sagittal maximum intensity projection and segmentation (middle), and 3D view of the vessel segmentation (bottom)

## Non-Invasive Imaging Techniques

### Magnetic Resonance Angiography (MRA)

Cerebral vasculature can be imaged using different types of MRI sequences that leverages the different magnetic properties of flowing blood and stationary tissues. Magnetic Resonance Angiography (MRA) is a specialized technique within MRI aimed at visualizing blood vessels. The fundamental principle of MRA involves exploiting the differences in signal properties between flowing blood and surrounding stationary tissues. This section elucidates how these differences are utilized to generate detailed images of the vasculature.Non-invasive MRA is a highly useful tool for imaging small vessels and for various other clinical uses (such as diagnosing CVDs such as stenosis, AVMs, stroke) (Park et al. 2018). MRA is specifically designed for exploiting these differences in blood and tissue magnetic properties using flow and signal encoding (Korosec, 2011).
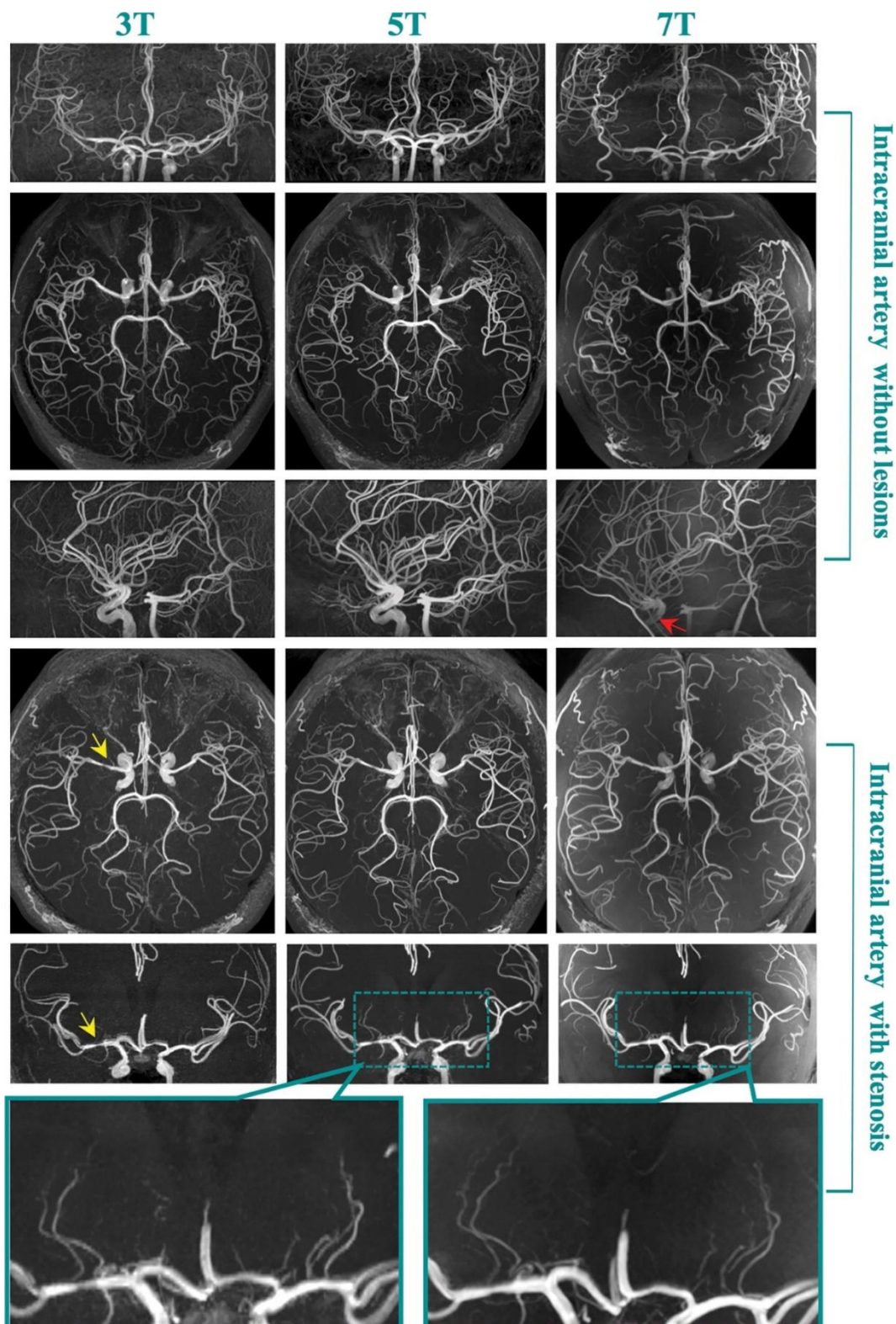
Fig. 3. From Zhang et al. 2023 (Fig. 4.) showing TOF-MRA at various field strengths highlighting large intracranial artery with and without lesions.

One such method is flow-related enhancement, also known as the time-of-flight effect. The concept is derived from the time lapse between the modification and detection of the flowing magnetization of blood (Kim & Parker, 2012). When blood flows into the imaging slice, it has not been subjected to previous RF pulses, unlike stationary tissues that have reached a steady state of magnetization. As a result, the inflowing blood has higher longitudinal magnetization, producing a stronger signal when excited by the RF pulse. This enhanced signal from the fresh blood allows for clear visualization of blood vessels (Kim & Parker, 2012). TOF-MRA can be divided into two categories: one which yields a high signal from flowing spins and a lower signal from stationary spins (from background tissue aka white blood) and two, which yields a strong signal from stationary spins (background tissue) and lower signal from flowing spins (aka black blood). The latter at UHF allows visualisation of small perforating arteries such as lenticulostriate arteries (Shao et al., 2021; Gorochowski & Staśkiewicz, 2017). For white blood imaging, background tissue can be suppressed using spoiled gradient echo sequence (SPGRE) with short TR as the spoiling saturates signal form static tissue and the TR is adjusted to be long enough for sufficient amount of blood to flow into imaging plane – this creates the contrast between static and flowing spins (Kim & Parker, 2012).

Another method is using Gradient Echo Pulse Sequences. These are preferred for MRA due to their sensitivity to the time-of-flight effect. In a gradient echo sequence, the high velocity of blood flow does not lead to significant signal loss because the moving spins only need to experience a single slice-selective RF pulse. Spatial encoding gradients (phase and frequency) are applied uniformly, ensuring accurate localization of signals from spins, whether they remain in the slice or move out before signal sampling. (Kuo et al. 2019)

In contrast, Spin Echo Pulse Sequences, though also applicable in MRA, are less effective for imaging high-velocity blood flow. The 180-degree RF pulse used for refocusing in spin echo sequences is less effective for moving spins, leading to rapid signal decay (high velocity signal loss). Nonetheless, new spins entering the slice still exhibit high longitudinal magnetization, providing a detectable signal, albeit less prominent than in gradient echo sequences (Lipton, 2014).

MRA typically involves imaging a stack of slices, where the inflow of unsaturated blood into the initial slices results in high signal intensity, clearly delineating the vessels. As blood flows through successive slices, it becomes increasingly saturated due to repeated RF pulses, reducing the flow-related enhancement, an effect known as the entry slice effect (Ballinger et al. 2024).

Flowing blood in the plane of the imaging slice can cause phase misregistration artifacts due to the differential timing between phase and frequency encoding, leading to a spatial shift in the signal (Larson et al. 1990). Understanding and correcting for this effect is essential for accurate vessel imaging. Utilizing higher magnetic field strengths can enhance the overall signal, including that from flowing blood, though this approach increases the signal from all tissues, not exclusively from blood flow. Thus, to maximize the visualization of blood vessels using time-of-flight MRA, gradient echo sequences become particularly effective at capturing the enhanced signal from inflowing blood due to its ability to differentiate high signal blood flow from lower signal stationary tissues (Lipton, 2014).

To form an image of a single slice the generated signals must come from spins present within the slice. It is possible to that by tipping the magnetization within slice of interest into the transverse plane to enable the receiver coil to detect it. By applying magnetic field gradient along with a specifically tailored RF pulse allows to image the slice (Korosec, 2019).

In clinical practice, the inferior most slices of a stack often show prominent flow-related enhancement because fresh, fully relaxed blood enters these slices with high longitudinal magnetization, providing a bright signal that clearly outlines the vasculature. MRA acquisition often involves interleaving slices, where slices are not acquired sequentially, leading to variations in the observed flow-related enhancement and complicating image interpretation. The highest velocity flow occurs at the centre of vessels, maintaining substantial flow-related enhancement deeper into the slice stack, while slower peripheral flow saturates earlier, resulting in reduced signal (Lipton, 2014).

MR vascular imaging can be easily implemented by manipulating standard GE sequencing parameters such as shortening TR and TE (Park et al. 2017). To improve image quality and vascular contrast, many methods such as MOTSA (multiple overlapping thin slab acquisition) (Parker et al. 1991a), TONE (titled optimised non-saturating excitation) (Atkinson et al. 1994), fast UHF MRA methods such as SENSE (sensitivity encoding), SMASH (simultaneous acquisition of spatial harmonics) and GRAPPA (generalised auto calibrating partial parallel acquisition) (Blaimer et al. 2004; Larkman and Nunes, 2007) are widely used.

MOTSA reduces saturation effects by decreasing the thickness of its three-dimensional (3D) imaging slabs. It also maintains volume coverage by using multiple slabs and then discarding overlapped slices when acquiring the final maximum intensity projection images.

The use of ramped RF excitation pulses, known as tilted optimized non-saturating excitation, generates uniform vessel signals within the image volume and can be applied to variable flip angles across the 3D acquisition volume. This approach was discussed in studies by Wu et al., (2007) and Nägele et al., (1995).
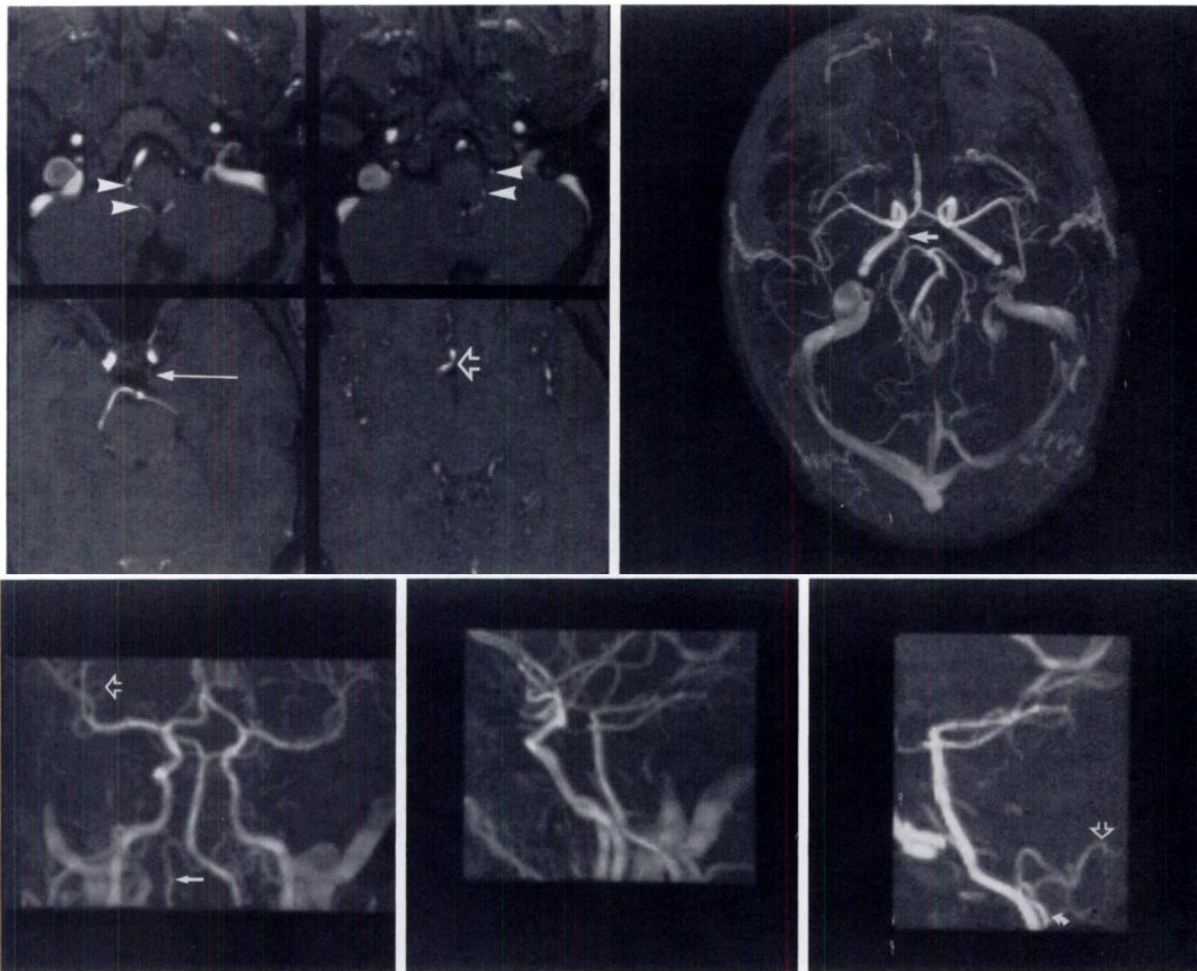


Fig. 4. From Parker et al. 1991 (Fig. 3.) MOTSA MRA showing PICA (top left), large PCA (top right), frontal (bottom left) and lateral (bottom middle) small right vertebral artery and lateral region of posterior fossa (bottom right).

Other than these methods to overcome SAR effects include VERSE (Schmitter et al., 2011) and segmented TOF MRA (Liu et al. 2021).

Vascular segmentation methods are used for delineating the vesicular structures in the brain. Normally manual segmentation (which could be done using the anatomical information) is difficult and time-consuming (Liu et al. 2021). There are 4 main categories for cerebrovascular segmentation: Segmentation based on pixel grayscale (Saleh et al. 2011; Gan et al. 2004), segmentation based on deformation model (Gooya et al. 2012; Cheng et al. 2015) and segmentation based on cerebral vessel enhancement (Frangi et al. 1998; Forkert et al. 2011).

Segmentation based on statistical methods (Hassouna et al. 2006; Wen et al. 2015), using this it is possible to distinguish high-intensity large cerebral vessels. However, small cerebral vessels are difficult to identify due to low intensity (Lesage et al. 2009; Zhao et al. 2017). Statistical methods commonly utilise eigenvalue of Hessian Matrix to identify cerebral vessels (Liu et al. 2021).

Cerebral vesicular characteristics can be distinguished from other brain tissues/structures by using different combination of eigenvalues corresponding to their respective characteristics. One such method which is widely used is the Frangi's Hessian method (Frangi et al., 1998). Another method proposed by Forkert et al. 2011 is the fuzzy-based enhancement of cerebral vessels that combine filtering of cerebral vessels and fuzzy logic-based method to improve segmentation of small and malformed cerebral vessels (Forkert et al. 2011). Another proposed method is using seed point detection, but this has normally been used with Frangi's Hessian matrix enhancement (Xiao et al. 2018). For detailed explanations on these methods, refer to (Frangi et al. 1998; Forkert et al. 2011; Gooya et al. 2012; Cheng et al. 2015).

Fast imaging MRA applications include parallel processing and compressed sensing techniques (Park et al. 2017). Parallel reconstructions algorithms (SMASH and GRAPPA), also called parallel MRI (pMRI) technique uses calculation and reconstruction of missing data from image-based (SENSE) and k-space based (GRAPPA and SMASH) domains (Park et al. 2017; Blaimer et al. 2004; Griswold et al. 2006). Compressed sensing methods (CS MRA) based on vessel energy spectrum has improved vascular contrast at the target vessels (Kang et al. 2016). The energy spectrum profile of each vessel can be utilized for variable density sampling patterns. These rapid imaging methods are now widely used for dynamic MRA applications, such as contrast-enhanced MRA images at 1.5T and 3T MRI (Gratz et al. 2016; Mende et al. 2007; Rapacchi et al. 2015). In the future, these techniques may be adapted for use in UHF 7T MRI for MRA applications.

In addition, recent focus has been on simultaneous multi-slice or multi-band imaging methods of UHF MRI systems, as well as 4D MR flow-sensitive techniques utilizing phase contrast MRA with vastly under sampled isotropic projection reconstruction to improve acquisition speed and SNR (Schrauben et al. 2014; Turk et al. 2007). Furthermore, field strength-dependent parallel imaging strategies using UHF MRI systems have been suggested for better acquisition speed and higher SNR, requiring precision in RF pulse design along with specialized hardware support such as coil sensitivity and B1 homogeneity. These applications show promise for vascular imaging in UHF MRA (Park et al. 2019).

Grochowski & Staśkiewicz (2017) provide a comparative analysis of various ultra-high field TOF-MRA techniques, highlighting differences based on the scanner used. It includes studies by several authors and details specifics such as manufacturer, coil type, flip angle, TE, TR, field of view (FOV), slices per slab, matrix size, voxel size, and acquisition time.

For instance, von Morze et al. (2007) utilized an eight-channel phased array receiver coil on a GE Healthcare scanner with a flip angle of 25 degrees, TE of 2.5 ms, and TR of 30 ms, achieving a voxel size of 0.63 x 0.8 x 0.1 mm³ over a 13-minute acquisition time. In contrast, studies using the MAGNETOM 7 T from Siemens Medical Solutions, like those by Maderwald et al. (2008) and Heverhagen et al. (2008), employed different coil configurations and imaging parameters, resulting in varied acquisition times and resolutions. These detailed parameters highlight the technical diversity and optimization strategies across different ultra-high field ToF-MRA setups. This information is useful for choosing the optimal parameters for designing neuroscientific studies or for BOLD modelling.

**Table. 1. Summary of Magnetic Resonance Angiography (MRA) Sequences and Techniques**

| Sequence | Description | References |
|---|---|---|
| *Time-of-Flight (TOF)* | Utilizes differences in longitudinal magnetization between flowing blood and stationary tissue. RF pulses selectively excite fresh inflowing blood, producing high signal. Differentiates between white blood (high signal from stationary tissue) and black blood (high signal from flowing blood). Effective for visualizing vessels due to enhanced blood flow contrast. Can be affected by entry slice effects and phase misregistration artifacts. | Kim & Parker, 2012; Gorochowski & Staśkiewicz, 2017 |
| *Gradient Echo* | Preferred for MRA due to sensitivity to time-of-flight effect. Minimizes signal loss from high-velocity blood flow. Uses uniform application of spatial encoding gradients (phase and frequency). Enables accurate localization of signals from moving spins within the slice. | Kuo et al. 2019 |
| *Spin Echo* | Less effective for high-velocity blood flow due to rapid signal decay from refocusing RF pulses. Detects new spins with high longitudinal magnetization, albeit less prominently compared to gradient echo sequences. Suitable for certain MRA applications but less sensitive to flowing spins. | Lipton, 2014 |
| *Spoiled Gradient Echo (SPGRE)* | Suppresses background tissue signal using short TR to saturate static tissue. Adjusts TR to allow sufficient inflow of blood into imaging plane, enhancing contrast between stationary and flowing spins. Improves visualization of blood vessels by differentiating between static and flowing spins. | Kim & Parker. 2012 |
| *Multiple Overlapping Thin Slab Acquisition (MOTSA)* | Reduces saturation effects by employing thinner 3D imaging slabs. Maintains volume coverage using multiple slabs and discarding overlapped slices for final maximum intensity projection images. Uses ramped RF excitation pulses for uniform vessel signals across 3D acquisition volume. | Parker et al. 1991 |

| | | |
|---|---|---|
| *Sensitivity Encoding (SENSE)* | Parallel reconstruction technique compensating for missing k-space data. Enhances imaging speed and resolution by utilizing image-based calculations. Widely used for fast MRA, improving acquisition times and spatial resolution. | Blaimer et al. 2004 |
| *Simultaneous Acquisition of Spatial Harmonics (SMASH)* | Parallel reconstruction technique using k-space based data. Similar to SENSE, enhances imaging speed and resolution by reconstructing missing data. Improves efficiency of MRA acquisitions, particularly useful for high-resolution scans | Larkman and Nunes, 2007 |
| *Generalized Auto-calibrating Partial Parallel Acquisition (GRAPPA)* | Parallel reconstruction method using k-space data to accelerate image acquisition. Calculates missing data points from neighboring acquired data. Provides faster MRA scans while maintaining image quality and spatial resolution. | Griswold et al. 2006 |
| *Compressed Sensing (CS MRA)* | Uses vessel energy spectrum for variable density sampling patterns. Improves vascular contrast and acquisition speed in dynamic MRA applications. Based on sparse representation of signals for high-quality image reconstruction. | Kang et al. 2016 |

For a more detailed overview on UHF ToF-MRA parameters, refer to the review by Gorochowski & Staśkiewicz, 2017.

### **Magnetic Resonance Venography**

Over the last several years, attention has been increasingly dedicated to non-invasive imaging of the cerebral venous drainage systems. MRV has emerged as one of the techniques capable of depicting venous vasculature providing insights into various CVDs and is also sensitive to detecting abnormal iron depositions in iron related CVDs such as Alzheimer's (Haacke et al. 2007).

MR susceptibility-weighted imaging (SWI) has recently demonstrated great clinical significance in the diagnosis of these CVDs by imaging the venous system especially at the sub-millimetre range without using contrast fluids (Reichenbach et al. 1998). Several MR venography (MRV) techniques have been developed to achieve superior contrast-to-noise ratio (CNR) between venous vessels and surrounding tissues including SWI (Haacke et al. 2004) and. more advanced image processing techniques, including true SWI (tSWI), quantitative susceptibility mapping (QSM), and susceptibility map-weighted imaging (SMWI), have emerged (Gho et al. 2014; Liu et al. 2014). Research utilizing ultra-high field (UHF) 7 Tesla MRI systems is actively investigating the optimal echo time (TE) to maximize the contrast between venous signals and brain tissue signals (Cosottini et al. 2015; Dixon et al. 2013; Koopmans et al. 2008; Kwan et al. 2016).

These studies demonstrate that higher magnetic field strengths can significantly improve the detection of small intracortical veins and other minute vascular details.
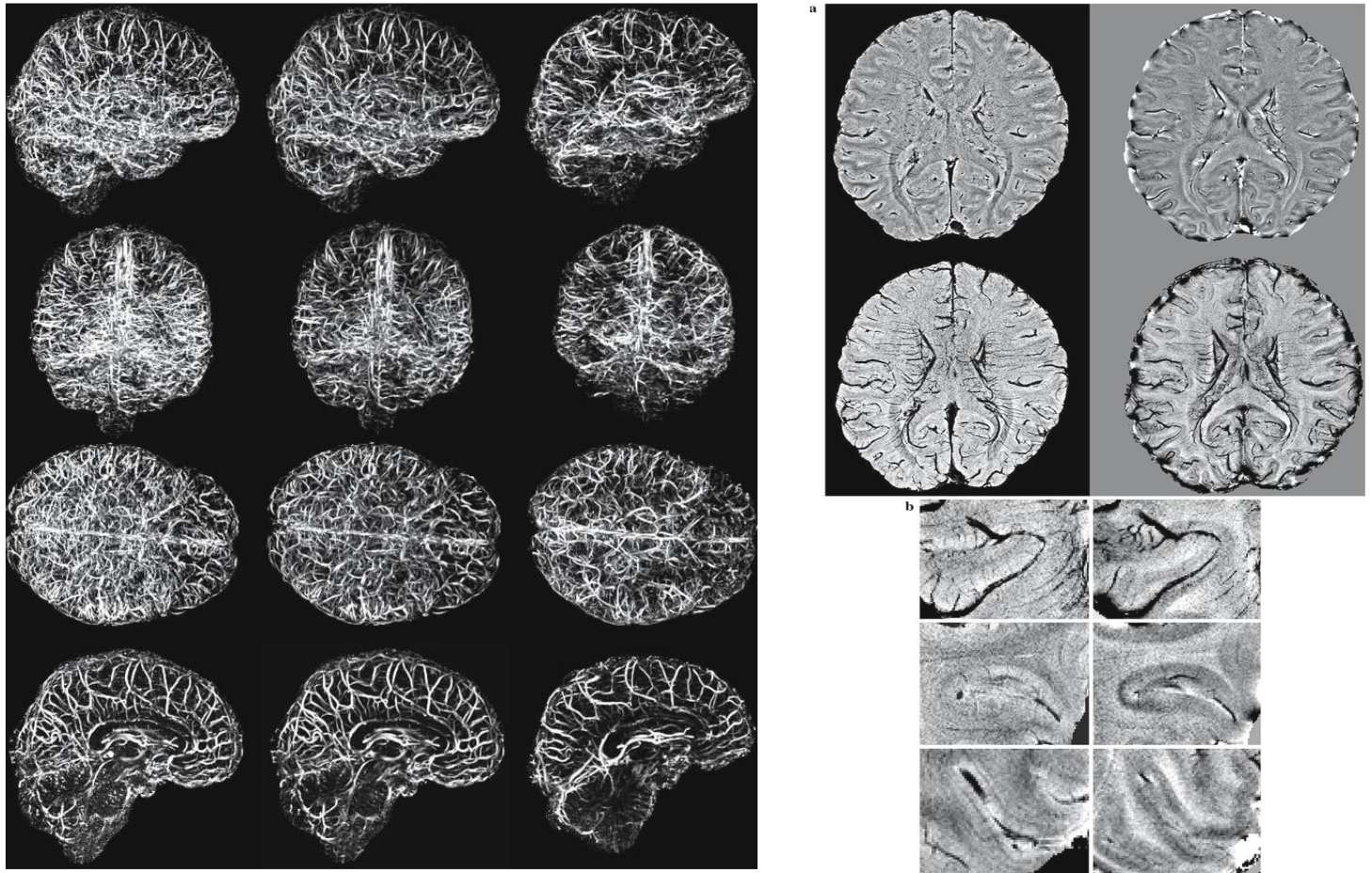


Fig. 5. From Koopmans et al. 2008 (Fig. 3; Fig. 5. resp.) (a) SWI-images acquired at 7T. The top row presents a single slice, while the bottom row shows a maximum intensity projection (mIP) over five slices. Zoomed-in sections from (a) revealing fine anatomical details, such as intracortical veins and the layered structure of grey matter. (c) Whole brain MR venograms using datasets acquired at 3 T with the Utrecht vesselness filter (first column) and after five iterations of the VED filter (second column). The third column presents the VED filtered dataset from the same volunteer acquired at 7 T.

## Automatic SWI Venography Segmentation

Susceptibility-weighted imaging (SWI) venography (Haacke et al. 2004; 2009) is a recent technique that exploits both the magnitude and phase of complex MRI signal to increase sensitivity to deoxygenated (venous) blood. This protocol can image cerebral veins with superior contrast and can image deep veins not visible on standard gadolinium contrast (Beriault et al. 2014). SWI enhances the visibility of venous structures by exploiting the magnetic susceptibility differences between deoxygenated blood in veins and oxygenated blood in arteries or surrounding tissues.

This creates a strong contrast in the images, where veins appear darker due to phase shifts caused by the magnetic susceptibility differences (Beriault et al. 2014).

Segmentation of SWI is difficult as it produces dense venograms that cannot be segmented using manual or semi-automatic methods within a reasonable time, and because SWI is also sensitive to iron-rich brain structures and to signal loss at inter-hemispheric fissure and air-tissue interfaces. Separation of surface veins and skull is also challenging because both structures are hypointense. (Beriault et al. 2015).

Existing segmentation methods include statistical methods, scale-space methods, and deformable models. Statistical methods hypothesize about vessel appearance relative to other tissues; rely on intensity distribution models and often use Finite Mixture Models (FMM) for classification (Beriault et al. 2015). Scale-space methods enhance vessel structures based on geometric properties like tubularity and elongation (Beriault et al 2015). Deformable models evolve an initial surface to fit the vascular tree but face challenges with SWI due to incomplete contrast and connectivity assumptions. (Beriault et al. 2015).

Accordingly, Beriault et al. (2015) developed a automated segmentation technique called Conditional Random Field (CRF) model that integrates multiple first and second order measures (also called potentials) such as appearance, shape, location, autologistic (Ising) interaction and data dependent interaction potentials to get a complete and automated segmentation of SWI venography datasets.

Conditional Random Fields (CRF) is a statistical modelling method used to segment structured data. Unlike traditional classification methods that treat each voxel independently, CRF considers the spatial dependencies between neighbouring voxels, aiming to assign a discrete label to each voxel based on the observed MRI data. This results in a dataset where each voxel is classified as either a vessel or other tissue (Beriault et al. 2015). The CRF model leverages the intensity differences and spatial relationships inherent in the SWI data.

Beriault et al. 2015 provide an overview of types of potentials used to achieve accurate segmentation. Appearance potentials utilize intensity information from the SWI data to model the likelihood of each voxel belonging to a vein. Veins typically appear darker on SWI images due to the susceptibility effects of deoxygenated blood, allowing the model to differentiate them from surrounding tissues and arteries.Shape potentials incorporate prior knowledge about the typical shapes and structures of veins, enabling the CRF model to recognize vein-like patterns and distinguish them from other anatomical structures.

Location potentials use anatomical information about the typical locations of veins in the brain, incorporating spatial priors to better identify regions where veins are likely to be present, thus reducing the likelihood of misclassifying arteries or other tissues as veins. To ensure spatial coherence, auto-logistic (Ising) interaction potentials encourage neighbouring voxels to have similar labels, maintaining the continuity of vein structures while suppressing noise and artifacts from surrounding tissues. Data-dependent interaction potentials model contextual dependencies between all pairs of neighbouring voxels, with an interaction term composed of a smoothness potential (also the Ising term) and a data-dependent edge potential. This combination achieves the goals of regularizing the segmentation and detecting finer veins. Optimization techniques such as Iterated Conditional Modes (ICM) and Graph Cuts ensure that the segmentation process balances accuracy and computational efficiency, refining the boundaries between veins, arteries, and other tissues for precise segmentation.
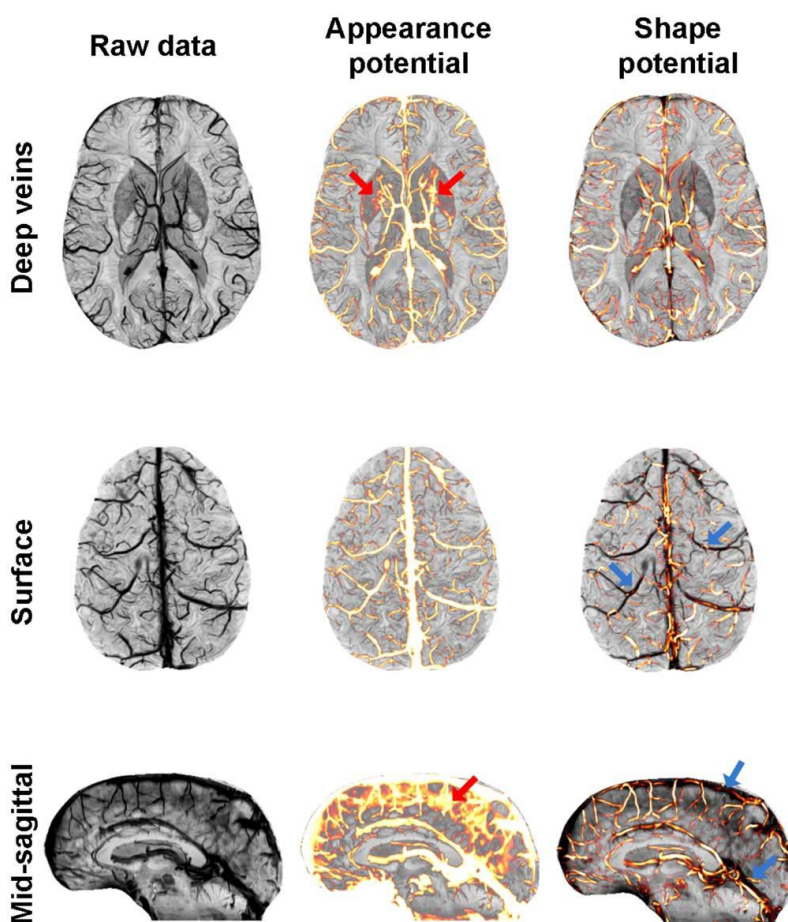


Fig. 6. From Beriault et al. 2015 (Fig. 1.) illustrating the appearance and Hessian-based shape potentials. The appearance potential is responsive to hypointense structures, including blood vessels, iron-rich lenticular nuclei, and signal loss at the inter-hemispheric fissure (indicated by red arrows). The shape potential identifies vasculature by detecting local tubularity within the data but may under-segment surface vessels and large sinuses in the mid-sagittal plane (indicated by blue arrows)

The CRF model exhibits sensitivity to susceptibility artifacts near air-tissue interfaces, particularly in the orbitofrontal cortex and inferior temporal lobes. This limitation is inherent to the SWI method itself, and incorporating additional location potentials could help exclude these artifacts from the final segmentation. Another limitation of the SWI acquisition strategy is that the second and fourth echoes are not flow compensated, which can lead to signal loss in large arterial vessels due to fast flow, potentially causing them to be mistaken for veins by the CRF. However, the use of 3 out of 5 flow-compensated echoes was found to be sufficient for robust preservation of arterial signal, at least in brain regions dorsal to the circle-of-Willis. In larger arteries below this level, SWI may not be the most convenient modality due to air-tissue interface susceptibility artifacts. (Beriault et al. 2015).

In this context, Magnetic Susceptibility Imaging becomes particularly relevant. Magnetic susceptibility is an innate property of tissues that describes how their atoms respond in a strong magnetic field, such as the paramagnetic effect of iron (Huck et al. 2019). This property can be imaged using Quantitative Susceptibility Mapping (QSM), which is primarily sensitive to myelin, iron deposition, and deoxygenated haemoglobin (dHb) in the brain (Langkammer et al. 2012; Stüber et al. 2014; Fan et al. 2014; Wang & Liu 2015). QSM can be used to image veins, as the presence of paramagnetic dHb molecules creates a difference in magnetic susceptibility between venous blood and surrounding tissue. Additionally, the quantitative susceptibility in each venous voxel is directly related to the Oxygen Extraction Fraction and the Cerebral Metabolic Rate of Oxygen through Fick's principle (Fan et al. 2014; Serres et al. 2015). Therefore, QSM is a powerful technique for studying the venous network, as it provides information about both venous structure and local metabolism (Huck et al. 2019).

Huck et al. (2019) initially manually segmented QSM images to identify venous structures based on their high susceptibility contrast. They segmented venous structures for each participant at multiple time points so that it captures the temporal variations and enhanced the accuracy of the venous maps. QSM can differentiate veins as they are filled with deoxyhaemoglobin, so they show up with higher susceptibility values on QSM images (Huck et al. 2019). This high contrast makes them stand out against surrounding tissues like white matter, grey matter, and cerebrospinal fluid (CSF).
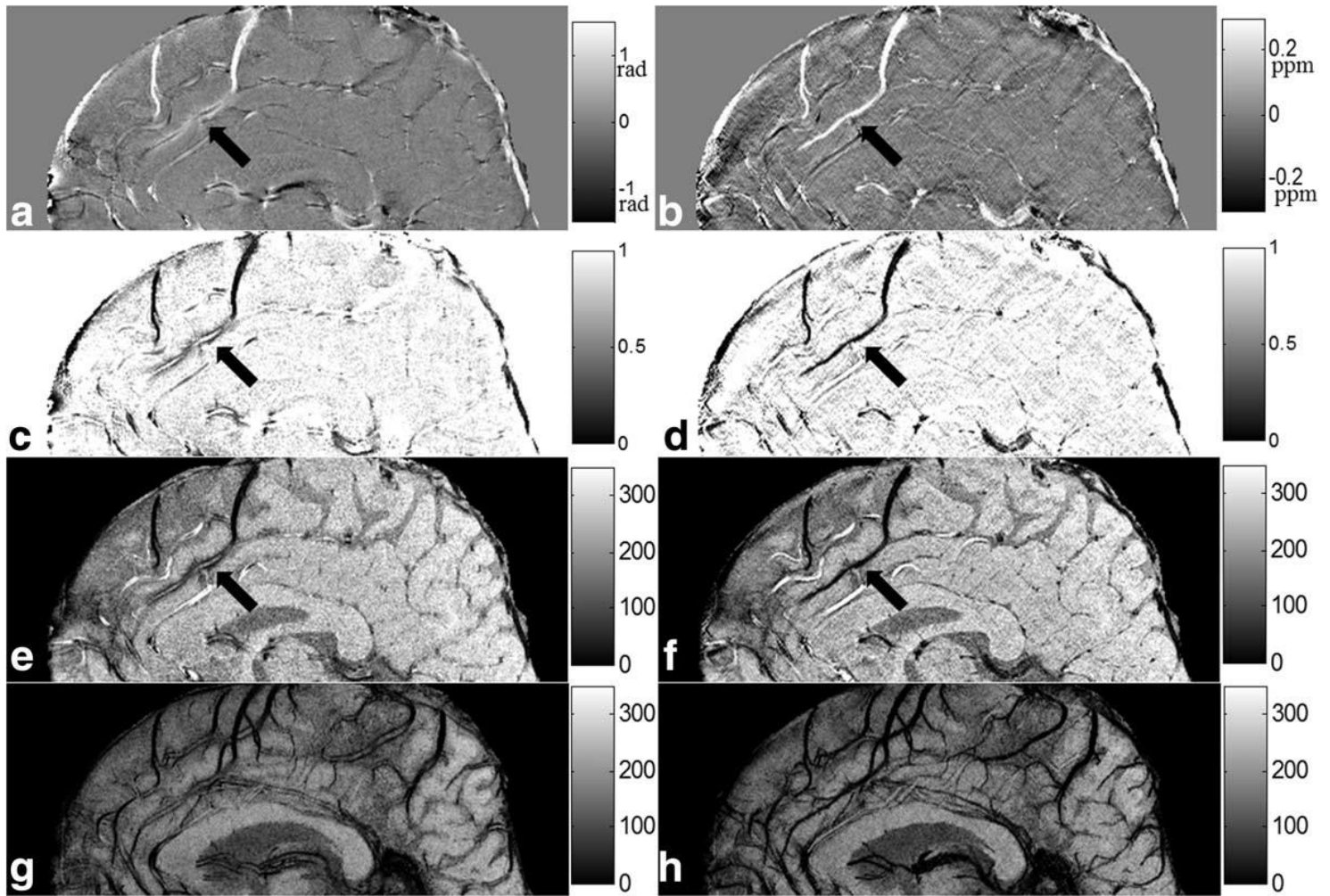
Fig. 7. From Liu et al. 2014 (Fig. 7), A sagittal view of a vein indicated by black arrows. (a) Phase image (from a left-handed system) shows effectively zero phase inside the vein, with visible outer field dipole effects. (b) Susceptibility maps depict the vein as uniformly bright. (c) Susceptibility weighting mask derived from the phase image (n = 4). (d) Susceptibility weighting mask derived from the susceptibility maps (x1 = 0, x2 = 0.45 ppm, n = 2). (e) SWI image displaying unsuppressed signal inside the vein. (f) tSWI image showing clear suppression of the vein, even at the magic angle. (g) Maximum intensity projection (mIP) of SWI in the sagittal direction. (h) mIP of tSWI in the sagittal direction. Notably, the vessels near the magic angle are well delineated in the tSWI data.

The delineation of venous structures at higher magnetic field strengths (7T) is clearer. In contrast, arteries contain oxygenated haemoglobin, which is diamagnetic resulting in lower susceptibility values on QSM images compared to veins. QSM can take advantage of the anatomical and functional differences between arteries and veins. (Huck et al. 2019). The Venous atlas reconstructed by Huck et al. (2019) also portray the possibility of combining QSM with other modalities like BOLD (Blood Oxygen Level Dependent) imaging to further enhance the distinction by exploiting the functional differences related to oxygenation levels during different physiological states.
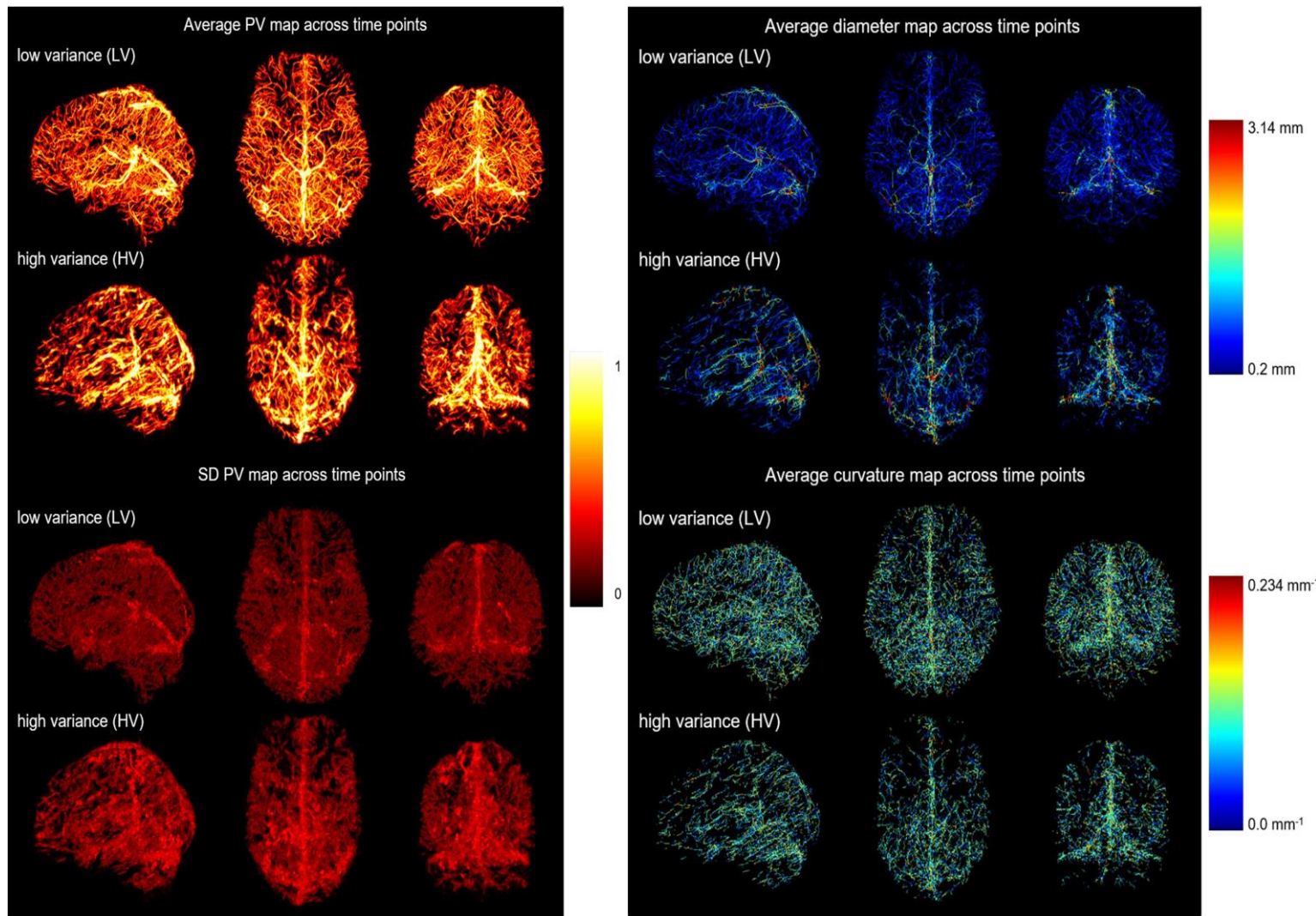
Fig. 8. From Huck et al. (2017) (Fig.2; Fig.5 resp.), venous brain atlas at 7T QSM maps.
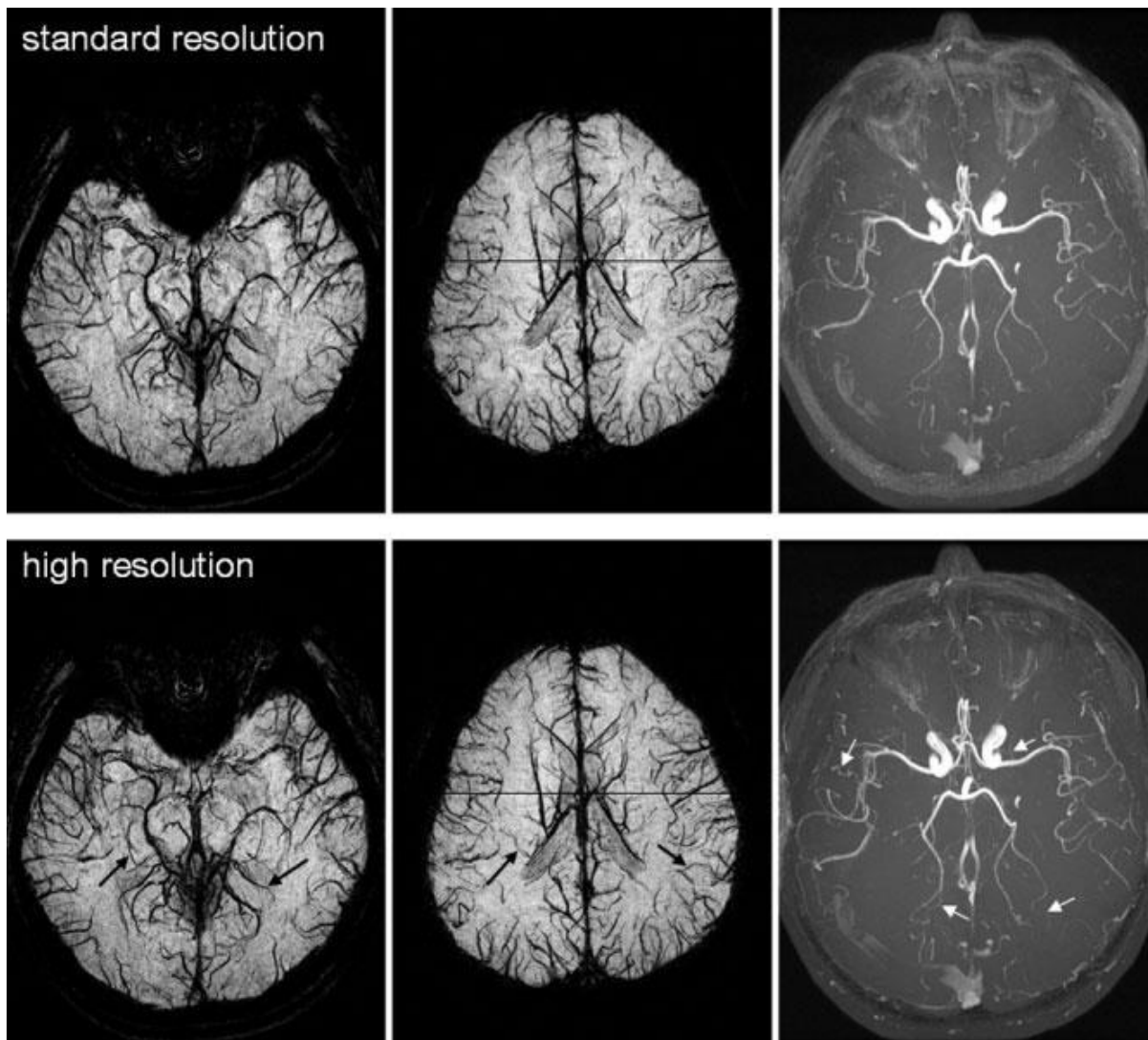
Fig. 9. From Du & Jin, 2008 (Fig.2), Projections of MRV and MRA data at different resolutions. The top row displays standard-resolution data ($0.78 \times 0.78 \times 1.6$ mm³). The bottom row shows high-resolution data ($0.52 \times 0.52 \times 1.6$ mm³). The high-resolution images enhance the contrast of veins (black arrows) and arteries (white arrows).

The following table summarizes the key methodological parameters used in various MR venography studies to aid in the identification of optimal parameters and methodologies for specific clinical and research applications.

**Table 2. Comparison of MRI Parameters and Techniques Across Various Studies for Brain Venous Vasculature Imaging**

| Parameter | Automated SWI Segmentation Using Conditional Random Fields (Beriault, 2015) | High resolution atlas of the venous brain vasculature from 7 T quantitative susceptibility maps (Huck et al. 2019) | MR venography of the human brain using susceptibility weighted imaging at very high field strength (Koopmans et al. 2008) | Simultaneous MR Angiography and Venography (MRAV) (Du & Jin, 2008) |
|---|---|---|---|---|
| MRI System | 3T Siemens TIM Trio | 7 T Siemens Magnetom (Siemens, Erlangen, Germany) | 7T & 3T (Siemens, Erlangen, Germany) | GE 3T scanner (Milwaukee, WI, USA) |
| Coil Used | 32-channel head coil | 32 channel Nova head coil | 3T: 8 channel head array 7T: CP head coil | Standard birdcage head coil |
| Sequences | 3D gradient -echo acquisition & MPRAGE | Multi Echo 3D GE FLASH & MP2RAGE (whole brain) | 3D gradient echo FLASH sequence | (for MRV) Dual echo MRAV Pulse sequence |
| TR | 3D: 48ms MPRAGE: 2300ms | FLASH: 29ms MP2RAGE: 5000ms | 3T: 35ms ; 7T: 22ms | 32ms |
| TE | 3D: 13-41ms MPRAGE: 2.98ms | FLASH: TE1: 8.16ms TE2: 18.35ms MP2RAGE: 2.45ms | 3T: 28ms ; 7T: 15ms | TE1: 3.1 ms (std), 4.1 ms (high) TE2: 24.5 ms |
| Flip Angle | 3D:17deg MPRAGE: 3deg | 1 / 2 = 5deg/3deg | 15 deg | 20 deg |
| Bandwidth | NA | 250Hz | 120Hz | 15.6 Hz |
| Voxel Size | 3D: 0.5 x 0.5 x 1 MPRAGE: 1 x 1 x 1 mm | FLASH: $260 \times 320 \times 256$ (0.6mm isotropic resolution) MP2RAGE: 320 x 320 x 240 (0.6mm isotropic resolution) | 3T:$0.57 \times 0.57 \times 1.25$mm3 (0.41 µl) 7T (whole brain): $0.57 \times 0.57 \times 1.25$mm3 (0.41µl) & (small structures) $0.27 \times 0.27 \times 1.5$mm3 (109 nl) | Standard resolution: 0.781 x 0.781 mm² (in-plane), 0.98 mm³ (volume) High resolution: 0.52 x 0.52 mm² (in-plane), 0.43 mm³ (volume) |
| Imaging processing | NA | multiscale vessel filter | Utrecht vesselness filter, Vessel enhancing diffusion (VED) filter | Projection onto convex sets (POCS) algorithm |
| Segmentation Method | Conditional Random Fields | Manual Segmentation | Not specified | Not specified |
| Scan time | 3D: 10min 24 s MPRAGE: 5min 30s | FLASH: 14min 22 s MP2RAGE: 10min 57 s | 3T: 15min ; 7T: 10min | Std Resolution: 7 minutes and 13 s High Resolution: 10 minutes and 46 s |

The integration of MRV with MRA has shown promising advancements in neuroimaging, as evidenced by studies like those of Du & Jin (2008) and Reichenbach et al. (2001). These studies highlight the potential of MRV not only as a clinical diagnostic tool but also as a means for BOLD modelling. The ability to simultaneously image MRA and MRV offers the possibility of developing a comprehensive and informed cerebral vasculature atlas informed of both the arterial and venous structures significantly enhancing our knowledge of cerebral anatomy and pathology.

**Discussion**

The present review discusses the measures to image cerebrovascular anatomy and potentially link it to measuring neural activity associated with increased blood flow and blood volume. The most commonly used method using vascular response to pinpoint underlying neural activity in the brain is BOLD measured using functional MRI. As mentioned before, BOLD is an indirect measure to understand underlying neural activity affected by the complexity of its sources of signal, factors that influence them such as oxygen metabolism, cerebral blood flow and blood volume (D'Esposito et al., 2003). BOLD contrast is used due to its ability to detect changes in deoxyhaemoglobin concentration ranging from small capillaries to large draining vessels (Duong et al., 2000; Menon et al., 1993), however its spatial and temporal specificity is brought into question as the measurement of blood flow, blood velocity and vessel diameter changes are not necessarily considered when extracting the signal. Even though alternative approaches for localisation of neural activity and measuring associated cerebral blood flow changes using ASL – fMRI is used (Kim, 1995; Kwong et al., 1995), its SNR is relatively low leading to low functional sensitivity.

Based on the techniques covered in the review, it is possible to image arteries and vessels, including pial arteries with diameters of 50-300μm detected using 7T TOF-MRA at 140 μm isotropic resolution (Bollman et al. 2021), micro vascular structures such as lenticulostriate arteries (Cho et al. 2008) as well as small venous vessels delineated using high-resolution 3T MR venography with T2*-weighted gradient-echo imaging at a spatial resolution of $0.5 \times 0.5 \times 1$ mm³ (Reichenbach et al, 2000).

In order to overcome the spatial limitations of BOLD, attempts to integrate information about the cerebrovascular anatomy into BOLD models have been made to enhance localization of the signal. The studies attempting to do so have so far been limited to rodent brain (VAN model: Gagnon et al. 2015; Gagnon et al. 2016) and not human brain. To this avail, this review discussed different ways in which we can map human cerebral vasculature.

As vast, complex and variable the cerebrovascular anatomy is, its possible to delineate the vesicular structures in-vivo and at high resolutions (Bollman et al. 2021; Cho et al. 2008; Reichenbach et al. 2000) based on the latest advancements in imaging sequences and processing algorithms.

The delineation of vessels can be potentially utilized to inform BOLD models and improve its localization accuracy. An implementation of this for rodent brain has been made by the VAN model (Gagnon et al. 2015; Gagnon et al. 2016) (and very recently for humans as well: see (Hartung et al. (n.d.)). The VAN model can perform complete reconstructions of rodent microvasculature up to the resolution of $\sim 600{\times}600{\times}600$ μm$^3$ and its input parameters are defined at single vessel level. If VAN model was to be extended to humans, it would need about the same resolution or higher for human vasculature, which has been achieved (as mentioned above). Studies discussed so far show that imaging in-vivo microvasculature and delineating locations and patterns of arteries and vessels is possible, and this information can be utilized to create priors for or to compliment BOLD models such as the VAN.

However, all of this is based on functional MRI and structural vascular imaging techniques. To clarify the imaging methods further, it can be bifurcated into two categories, direct structural measures such as conventional MRI, MRA and MRV; and indirect functional measures such as fMRI, BOLD contrast, VASO, ASL, fMRA and fMRV. Even though functional means tend of rely heavily on indirect measures like BOLD or VASO, in our opinion much reliable measures such as fMRA and fMRV have been proposed over two decades ago and not explored as much. The latter methods can be more reliable due to its direct relation to vasculature as these signals come from them and can provide a much closer link to neural activity, limiting the possibility of bias.

Indirect measures like BOLD are argued to reflect local processing of neural inputs rather and output signal as it arises from paramagnetic deoxyhaemoglobin in venous blood allowing real-time mapping of brain oxygenation (Logothetis, 2002; Ogawa et al. 1990). This indirect nature raises concerns about its interpretability (Nair, 2005). Studies in both anesthetized and awake monkeys have shown that local field potentials (LFPs) are better predictors of BOLD signals than multi-unit or single-unit activity (Logothetis, 2002; Goense & Logothetis, 2008). Specifically, LFPs in the 20-60 Hz range, likely related to neuromodulation, explain the largest portion of BOLD signal variance in alert animals (Goense & Logothetis, 2008). This suggests that BOLD primarily reflects the input and processing of neuronal activity within a region, rather than its output (Logothetis, 2002).

On the other hand, VASO fMRI measures changes in cerebral blood volume (CBV) during neural activation (Lu & Zijl, 2012). Unlike BOLD fMRI, VASO relies on nulling blood signals while maintaining tissue signals, resulting in a signal decrease during activation due to increased CBV (Lu et al., 2003). However, VASO's primary drawback is low contrast-to-noise ratio due to small signal changes from inverted blood (Wu et al. 2008). VASO also suffers from limited data acquisition efficiency, restricting imaging coverage and achievable spatial and temporal resolution (L. Huber et al. 2018). The technique requires accurate estimation of resting CBV and consideration of cerebrospinal fluid (CSF) contributions to signal changes, which can complicate interpretation of results (Scouten & Constable, 2007).

Similarly, ASL provides quantitative measures of network physiology and metabolism (Jann et al., 2015). It measures cerebral blood flow using arterial water as an endogenous tracer (Borogovac & Asllani, 2012a). While ASL provides reliable absolute quantification of cerebral blood flow with higher spatial and temporal resolution than other techniques, its routine application has been limited due to theoretical complexities and technical challenges (Borogovac & Asllani, 2012b). Compared to BOLD fMRI, ASL shows no differences in activation localization but exhibits distinct temporal characteristics (Federspiel et al. 2006).

Direct structural means for imaging vasculature such as MRA and MRV so far has only been used to visualise arteries and veins respectively. However, these sequences don't necessarily have to be used only for visualising the vasculature. Due to its direct link to vasculature, its functional sequences allow to image vasculature as well as pinpoint the location of neural activation identified by blood flow, volume, velocity changes. The said functional means – fMRA and fMRV was proposed and demonstrated by Zang Hee Cho and colleagues in 2008 & Lee and colleagues in 2015.

Cho et al. 2008 highlighted the capability of fMRA to directly observe changes in individual blood vessels in response to neural activity. This method offered higher spatial resolution and sensitivity than conventional fMRI, allowing accurate localization of neural activation sites. According to the first study conducted by Cho et al. (2008), diameter changes in peripheral vessels near neural activation sites were larger than those in distal vessels indicating greater vasodilation in smaller vessels during functional brain activity. The vessel diameter change detected was about 80% near terminal to 30% at the distal side during the task (Cho et al. 2008; refer to Fig.6).

Cho and colleagues followed their fMRA approach with fPCA (Functional Phase Contrast Angiography) or PC (phase contrast) MRA in 2010 (Kang et al. 2010). fMRA primarily focuses on direct visualisation of vascular responses like vessel dilation during neural activity (Cho et al 2008).

However, it does not provide quantitative information about blood flow and velocity. To address this issue, Kang and colleagues developed PC fMRA to measure quantitative blood velocity changes.

PC MRA achieves this by analysing circular regions of interest (ROIs) in the vessel segments and comparing the velocity changes between rest and stimulation conditions. This method allows for the measurement of dynamic vascular changes in both intensity and velocity in small cerebral arteries (Kang et al. 2010). Their results further indicate that PC MRA data can supply data similar to fMRA data acquired with TOF-MRA imaged at 3T. However, overall visualisation of vessels using TOF MRA was more advanced compared to PC MRA. fMRA was also further applied to resting state studies to provide information about the vascular effects in the brain during resting state, which can be particularly useful for investigating cerebrovascular diseases (Cho et al. 2015).
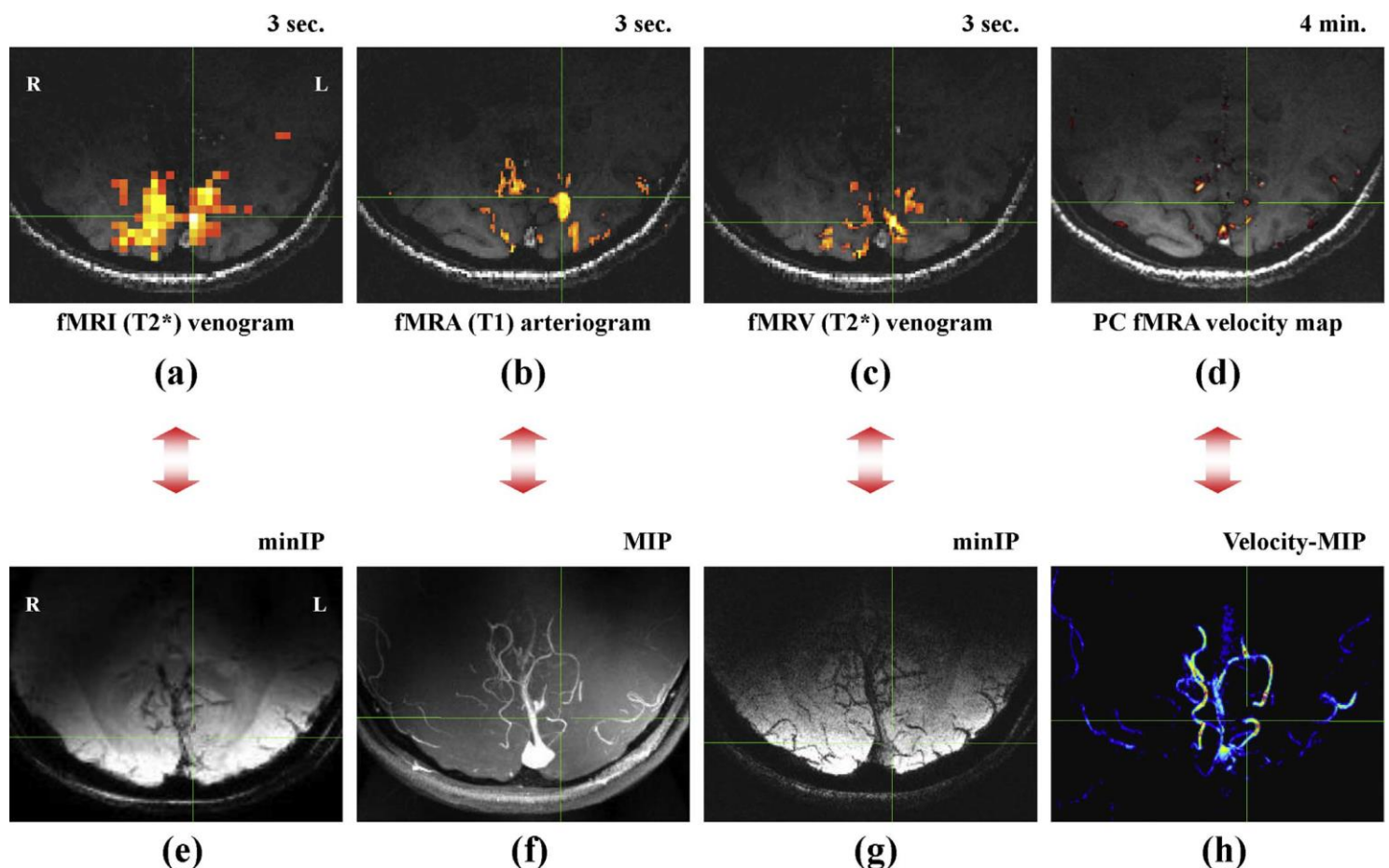


Fig. 10.  From Park et al. 2018 (Fig. 4), Comparison of resultant images during visual stimulation from different imaging techniques: (a) Conventional BOLD fMRI (T2*), (b) fMRA (T1), (c) fMRV (T2*), (d) PC fMRA velocity map. The vascular functional techniques highlight that fMRA, fMRV, and PC fMRA provide significantly superior resolution compared to conventional BOLD fMRI, suggesting potential for broader applications in functional blood flow imaging

With respect to venous visualisation and observation of venous dynamics, Lee and colleagues developed fMRV technique in 2015 to examining these changes, particularly blood oxygenation within cerebral veins during different conditions such as resting and stimulation (Lee et al. 2015). MRV is typically used to image venous malformations and SWI being the most prevalent techniques for the same (Haacke et al, 2004). The study by Lee et al. (2015) utilized a 7T MRI and the Time-resolved angiography With Stochastic Trajectories (TWIST) method to get a high temporal resolution of 3 seconds during visual stimulation. Due to a high temporal resolution, they were able to detect dynamic changes in blood oxygenation within the cerebral veins. Their study indicated fMRV's performance to be superior to SWI in detecting signal changes in venous vessels. fMRV showed signal changes between resting and stimulation conditions in venous vessels more clearly than SWI. The study demonstrated that dynamic changes in venous vessel oxygenation signals observed in the 3-second measurement windows, with an average increase in venous signal intensity of $6.86 \pm 0.82\%$ during stimulation relative to the resting condition. This indicates that fMRV can more effectively visualize individual venous vessel blood oxygenation changes during visual stimulation compared to SWI (Lee et al. 2015).

In conclusion, while BOLD fMRI remains the predominant technique for functional brain mapping, other vascular-based imaging methods, such as fMRA and fMRV, can provide complementary and more detailed information about blood dynamics to enhance our understanding and localization of neural activity. Furthermore, integrating these indirect vascular measures with computational models like the VAN model can further improve the accuracy of localizing neural activity and characterizing neurovascular coupling.

Although the original VAN modelling was based on rodent vascular structures, it has recently been extended to the human cortex (Hartung et al. (n.d.)). The human VAN model generated realistic vascular anatomical networks by incorporating topological and anatomical data of human vasculature. However, the results indicate that the human VAN model did not adequately capture the hemodynamic response, likely due to the lack of information about single-vessel dilation in humans. To address this limitation, fMRA sequence proposed by Cho et al. (2008) that focuses on vessel dilation during neural activity could possibly be used to get information about the same in humans.

This coupled with a series of imaging studies using fMRA / PC MRA and fMRV could be conducted to measure vascular dynamics more directly. Additionally, creating a comprehensive cerebrovascular atlas or maps, including both arterial and venous structures, could be used as priors for improving the accuracy of BOLD modelling algorithms.
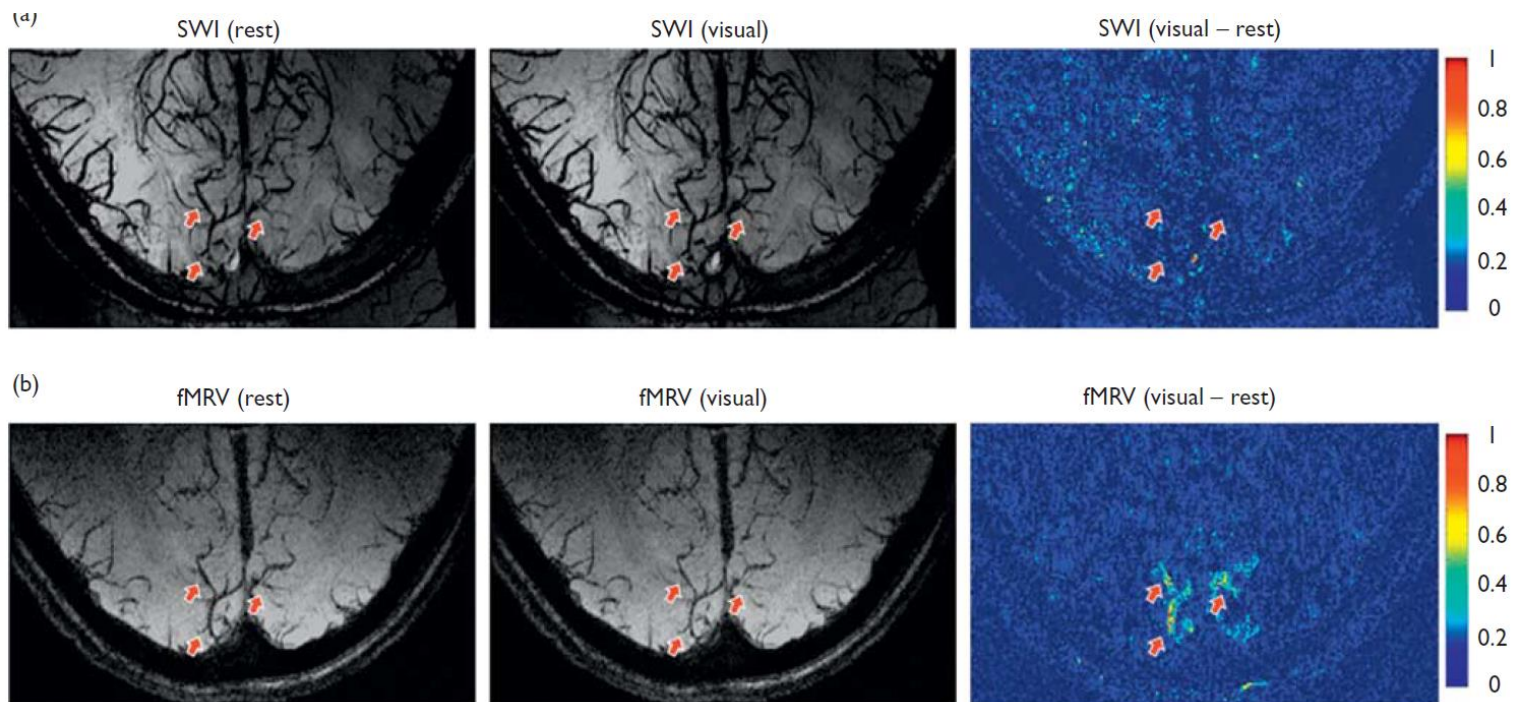
Fig. 11. From Lee et al. 2015 (Fig. 3), Comparison of functional imaging with SWI and MRV. images from SWI (a) and fMRV (b) during resting and stimulation conditions, along with their subtraction images. In both sets (a and b), red arrows indicate the predominant venous vessels responding to stimulation. The color bar represents the subtraction values between resting and stimulation sessions.

**Table 3: Summary of fMRA and fMRV Sequences and Techniques**

| Parameter | Functional MR angiography with 7.0 T Is direct observation of arterial response during neural activity possible? (Cho et al. 2008) | Functional MR angiography using phase contrast imaging technique at 3T MRI (Kang et al. 2010) | Imaging method for changes in venous dynamics: a preliminary study (Lee et al. 2015) |
|---|---|---|---|
| MRI System | 7 T Siemens Magnetom (Siemens, AG, Berlin, Germany) | 3 T MRI scanner (Allegra, Siemens, Germany) | 7T (Siemens, Erlangen, Germany) |
| Coil Used | Custom Coil | Custom Coil | Quadrature transmit/receive surface RF coil |
| Sequences | 3D FLASH GE TOF-MRA | PC MRA: NA TOF MRA: 3D FLASH GE | TWIST (time-resolved angiography with interleaved stochastic trajectories) |
| TR | 14ms | PC MRA: 43.6ms TOF MRA: 20ms | fMRV: 13.96ms SWI: 25ms |
| TE | 3.7ms | PC MRA: 6.7ms TOF MRA: 3.1ms | fMRV: 11ms SWI: 12ms |
| Flip Angle | 25deg | PC MRA: 30deg TOF MRA: 30deg | fMRV: 5deg SWI: 25deg |
| Bandwidth | NA | NA | fMRV: 590Hz SWI: 80Hz |
| Voxel Size | $0.70 \times 0.70 \times 1.00$ mm³. | $0.67 \times 0.67 \times 0.67$ mm³. | $0.5 \times 0.5 \times 0.5$ mm³ |
| Scan time | Stimulus scan: 2min 47 sec Rest scan: 15min | PC fMRA: Stimulus scan: 3min 26sec Rest scan: 3min 26sec TOF MRA: 1min 40sec | fMRV: 3sec SWI: 2min 35sec |

**References:**

Atkinson, D., Brant-Zawadzki, M., Gillan, G., Purdy, D., & Laub, G. (1994). Improved MR angiography: Magnetization transfer suppression with variable flip angle excitation and increased resolution. Radiology, 190(3), 890–894. https://doi.org/10.1148/radiology.190.3.8115646

Ballinger J, Campos A, Murphy A, Entry slice phenomenon. Reference article, Radiopaedia.org (Accessed on 20 May 2024) https://doi.org/10.53347/rID-22004

Bell, R., Severson, M. A., & Armonda, R. A. (2009). Neurovascular Anatomy: A Practical Guide. Neurosurgery Clinics of North America, 20(3), 265–278. https://doi.org/10.1016/j.nec.2009.04.012

Bériault, S., Sadikot, A. F., Alsubaie, F., Drouin, S., Collins, D. L., & Pike, G. B. (2014). Neuronavigation using susceptibility-weighted venography: Application to deep brain stimulation and comparison with gadolinium contrast: Technical note. Journal of Neurosurgery, 121(1), 131–141. https://doi.org/10.3171/2014.3.JNS131860

Beriault, S., Xiao, Y., Collins, D. L., & Pike, G. B. (2015). Automatic SWI Venography Segmentation Using Conditional Random Fields. IEEE Transactions on Medical Imaging, 34(12), 2478–2491. https://doi.org/10.1109/TMI.2015.2442236

Blaimer, M., Breuer, F., Mueller, M., Heidemann, R. M., Griswold, M. A., & Jakob, P. M. (2004). SMASH, SENSE, PILS, GRAPPA: How to Choose the Optimal Method. Topics in Magnetic Resonance Imaging, 15(4), 223–236. https://doi.org/10.1097/01.rmr.0000136558.09801.dd

Blatter, D. D., Parker, D. L., & Robison, R. O. (1991). Cerebral MR angiography with multiple overlapping thin slab acquisition. Part I. Quantitative analysis of vessel visibility. Radiology, 179(3), 805–811. https://doi.org/10.1148/radiology.179.3.2027996

Bradley, W. G. (Ed.). (2004). *Neurology in clinical practice*. Butterworth-Heinemann.

Bollmann, S., & Barth, M. (2021). New acquisition techniques and their prospects for the achievable resolution of fMRI. Progress in Neurobiology, 207, 101936. https://doi.org/10.1016/j.pneurobio.2020.101936

Bollmann, S., Mattern, H., Bernier, M., Robinson, S. D., Park, D., Speck, O., & Polimeni, J. R. (2022). Imaging of the pial arterial vasculature of the human brain in vivo using high-resolution 7T time-of-flight angiography. eLife, 11, e71186. https://doi.org/10.7554/eLife.71186

Borogovac, A., & Asllani, I. (2012a). Arterial Spin Labeling (ASL) fMRI: Advantages, Theoretical Constrains and Experimental Challenges in Neurosciences. International Journal of Biomedical Imaging, 2012, 1–13. https://doi.org/10.1155/2012/818456

Borogovac, A., & Asllani, I. (2012b). Erratum to "Arterial Spin Labeling (ASL) fMRI: Advantages, Theoretical Constrains and Experimental Challenges in Neurosciences". International Journal of Biomedical Imaging, 2012, 1–1. https://doi.org/10.1155/2012/658101

Boxerman (a), J. L., Bandettini, P. A., Kwong, K. K., Baker, J. R., Davis, T. L., Rosen, B. R., & Weisskoff, R. M. (1995). The intravascular contribution to fmri signal change: Monte carlo modeling and diffusion-weighted studies in vivo. Magnetic Resonance in Medicine, 34(1), 4–10. https://doi.org/10.1002/mrm.1910340103

Boxerman (b), J. L., Hamberg, L. M., Rosen, B. R., & Weisskoff, R. M. (1995). Mr contrast due to intravascular magnetic susceptibility perturbations. Magnetic Resonance in Medicine, 34(4), 555–566. https://doi.org/10.1002/mrm.1910340412

Buxton, R. B., Uludağ, K., Dubowitz, D. J., & Liu, T. T. (2004). Modeling the hemodynamic response to brain activation. NeuroImage, 23, S220–S233. https://doi.org/10.1016/j.neuroimage.2004.07.013

Carpenter, M. B. (1954). THE ANTERIOR CHOROIDAL ARTERY: Its Origins, Course, Distribution, and Variations. A.M.A. Archives of Neurology & Psychiatry, 71(6), 714. https://doi.org/10.1001/archneurpsyc.1954.02320420042005

Chandra, A., Li, W., Stone, C., Geng, X., & Ding, Y. (2017). The cerebral circulation and cerebrovascular disease I: Anatomy. Brain Circulation, 3(2), 45. https://doi.org/10.4103/bc.bc_10_17

Cheng, Y., Hu, X., Wang, J., Wang, Y., & Tamura, S. (2015). Accurate Vessel Segmentation With Constrained B-Snake. IEEE Transactions on Image Processing, 24(8), 2440–2455. https://doi.org/10.1109/TIP.2015.2417683

Cho, Z.-H., Kang, C.-K., Han, J.-Y., Kim, S.-H., Park, C.-A., Kim, K.-N., Hong, S.-M., Park, C.-W., & Kim, Y.-B. (2008). Functional MR angiography with 7.0 T. NeuroImage, 42(1), 70–75. https://doi.org/10.1016/j.neuroimage.2008.05.003

Cosottini, M., Frosini, D., Pesaresi, I., Donatelli, G., Cecchi, P., Costagli, M., Biagi, L., Ceravolo, R., Bonuccelli, U., & Tosetti, M. (2015). Comparison of 3T and 7T Susceptibility-Weighted Angiography of the Substantia Nigra in Diagnosing Parkinson Disease. American Journal of Neuroradiology, 36(3), 461–466. https://doi.org/10.3174/ajnr.A4158

De Freitas, G. R., Christoph, D. D. H., & Bogousslavsky, J. (2008). Chapter 22 Topographic classification of ischemic stroke. In Handbook of Clinical Neurology (Vol. 93, pp. 425–452). Elsevier. https://doi.org/10.1016/S0072-9752(08)93022-0

D'Esposito, M., Deouell, L. Y., & Gazzaley, A. (2003). Alterations in the BOLD fMRI signal with ageing and disease: A challenge for neuroimaging. Nature Reviews Neuroscience, 4(11), 863–872. https://doi.org/10.1038/nrn1246

Dixon, J. E., Simpson, A., Mistry, N., Evangelou, N., & Morris, P. G. (2013). Optimisation of T 2 * -weighted MRI for the detection of small veins in multiple sclerosis at 3 T and 7 T. European Journal of Radiology, 82(5), 719–727. https://doi.org/10.1016/j.ejrad.2011.09.023

Drake, R., Vogl, A. W., & Mitchell, A. W. (2015). *Gray's anatomy for students E-book*. Elsevier Health Sciences.

Du, Y. P., & Jin, Z. (2008). Simultaneous acquisition of MR angiography and venography (MRAV). Magnetic Resonance in Medicine, 59(5), 954–958. https://doi.org/10.1002/mrm.21581

Duong, T. Q., Silva, A. C., Lee, S.-P., & Kim, S.-G. (2000). Functional MRI of calcium-dependent synaptic activity: Cross correlation with CBF and BOLD measurements. Magnetic Resonance in Medicine, 43(3), 383–392. https://doi.org/10.1002/(SICI)1522-2594(200003)43:3<383::AID-MRM10>3.0.CO;2-Q

Duvernoy, H. M., Delon, S., & Vannson, J. L. (1981). Cortical blood vessels of the human brain. Brain Research Bulletin, 7(5), 519–579. https://doi.org/10.1016/0361-9230(81)90007-1

Fan, A. P., Bilgic, B., Gagnon, L., Witzel, T., Bhat, H., Rosen, B. R., & Adalsteinsson, E. (2014). Quantitative oxygenation venography from MRI phase: Quantitative Oxygenation Venography. Magnetic Resonance in Medicine, 72(1), 149–159. https://doi.org/10.1002/mrm.24918

Federspiel, A., Müller, T. J., Horn, H., Kiefer, C., & Strik, W. K. (2006). Comparison of spatial and temporal pattern for fMRI obtained with BOLD and arterial spin labeling. Journal of Neural Transmission, 113(10), 1403–1415. https://doi.org/10.1007/s00702-006-0434-5

Feekes, J. A., Hsu, S., Chaloupka, J. C., & Cassell, M. D. (2005). Tertiary microvascular territories define lacunar infarcts in the basal ganglia. Annals of Neurology, 58(1), Article 1. https://doi.org/10.1002/ana.20505

Ferro, J. M., & Canhão, P. (2014). Cerebral Venous Sinus Thrombosis: Update on Diagnosis and Management. Current Cardiology Reports, 16(9), 523. https://doi.org/10.1007/s11886-014-0523-2

Forkert, N. D., Schmidt-Richberg, A., Fiehler, J., Illies, T., Möller, D., Handels, H., & Säring, D. (2011). Fuzzy-based Vascular Structure Enhancement in Time-of-Flight MRA Images for Improved Segmentation. Methods of Information in Medicine, 50(01), 74–83. https://doi.org/10.3414/ME10-02-0003

Frangi, A. F., Niessen, W. J., Vincken, K. L., & Viergever, M. A. (1998). Multiscale vessel enhancement filtering. In W. M. Wells, A. Colchester, & S. Delp (Eds.), Medical Image Computing and Computer-Assisted Intervention—MICCAI'98 (Vol. 1496, pp. 130–137). Springer Berlin Heidelberg. https://doi.org/10.1007/BFb0056195

Gagnon, L., Sakadžić, S., Lesage, F., Musacchia, J. J., Lefebvre, J., Fang, Q., Yücel, M. A., Evans, K. C., Mandeville, E. T., Cohen-Adad, J., Polimeni, J. R., Yaseen, M. A., Lo, E. H., Greve, D. N., Buxton, R. B., Dale, A. M., Devor, A., & Boas, D. A. (2015b). Quantifying the Microvascular Origin of BOLD-fMRI from First Principles with Two-Photon Microscopy and an Oxygen-Sensitive Nanoprobe. The Journal of Neuroscience, 35(8), 3663–3675. https://doi.org/10.1523/JNEUROSCI.3555-14.2015

Gagnon, L., Smith, A. F., Boas, D. A., Devor, A., Secomb, T. W., & Sakadžić, S. (2016). Modeling of Cerebral Oxygen Transport Based on In vivo Microscopic Imaging of Microvascular Network Structure, Blood Flow, and Oxygenation. Frontiers in Computational Neuroscience, 10. https://doi.org/10.3389/fncom.2016.00082

Ghika, J. A. (1990). Deep Perforators From the Carotid System: Template of the Vascular Territories. Archives of Neurology, 47(10), 1097. https://doi.org/10.1001/archneur.1990.00530100063014

Gho, S., Liu, C., Li, W., Jang, U., Kim, E. Y., Hwang, D., & Kim, D. (2014). Susceptibility map-weighted imaging (SMWI) for neuroimaging. Magnetic Resonance in Medicine, 72(2), 337–346. https://doi.org/10.1002/mrm.24920

Goense, J. B. M., & Logothetis, N. K. (2008). Neurophysiology of the BOLD fMRI Signal in Awake Monkeys. Current Biology, 18(9), 631–640. https://doi.org/10.1016/j.cub.2008.03.054

Gooya, A., Liao, H., & Sakuma, I. (2012). Generalization of geometrical flux maximizing flow on Riemannian manifolds for improved volumetric blood vessel segmentation. Computerized Medical Imaging and Graphics, 36(6), 474–483. https://doi.org/10.1016/j.compmedimag.2012.04.007

Gratz, M., Schlamann, M., Goericke, S., Maderwald, S., & Quick, H. H. (2017). Evaluation of fast highly undersampled contrast-enhanced MR angiography (sparse CE-MRA) in intracranial applications – initial study. European Radiology, 27(3), 1004–1011. https://doi.org/10.1007/s00330-016-4398-z

Griswold, M. A., Breuer, F., Blaimer, M., Kannengiesser, S., Heidemann, R. M., Mueller, M., Nittka, M., Jellus, V., Kiefer, B., & Jakob, P. M. (2006). Autocalibrated coil sensitivity estimation for parallel imaging. NMR in Biomedicine, 19(3), 316–324. https://doi.org/10.1002/nbm.1048

Grochowski, C., & Staśkiewicz, G. (2017). Ultra high field TOF-MRA: A method to visualize small cerebral vessels. 7 T TOF-MRA sequence parameters on different MRI scanners – Literature review. Neurologia i Neurochirurgia Polska, 51(5), 411–418. https://doi.org/10.1016/j.pjnns.2017.06.011

Gupta, B., Yadav, R., Singhal, M., Kadam, N., Gehlot, K., & Singh, R. (2016). A rare case report of bilateral internal carotid artery hypoplasia in postpartum female: Clinical spectrum and role of various modalities in diagnosis. Brain Circulation, 2(2), 99. https://doi.org/10.4103/2394-8108.186286

Haacke, E. M., Ayaz, M., Khan, A., Manova, E. S., Krishnamurthy, B., Gollapalli, L., Ciulla, C., Kim, I., Petersen, F., & Kirsch, W. (2007). Establishing a baseline phase behavior in magnetic resonance imaging to determine normal vs. Abnormal iron content in the brain. Journal of Magnetic Resonance Imaging, 26(2), 256–264. https://doi.org/10.1002/jmri.22987

Haacke, E. M., Mittal, S., Wu, Z., Neelavalli, J., & Cheng, Y.-C. N. (2009). Susceptibility-Weighted Imaging: Technical Aspects and Clinical Applications, Part 1. American Journal of Neuroradiology, 30(1), 19–30. https://doi.org/10.3174/ajnr.A1400

Haacke, E. M., Xu, Y., Cheng, Y. N., & Reichenbach, J. R. (2004a). Susceptibility weighted imaging (SWI). Magnetic Resonance in Medicine, 52(3), 612–618. https://doi.org/10.1002/mrm.20198

Haacke, E. M., Xu, Y., Cheng, Y. N., & Reichenbach, J. R. (2004b). Susceptibility weighted imaging (SWI). Magnetic Resonance in Medicine, 52(3), 612–618. https://doi.org/10.1002/mrm.20198

Hamoir, X. L., Grandin, C. B., Peeters, A., Robert, A., Cosnard, G., & Duprez, T. (2004). MRI of hyperacute stroke in the AChA territory. European Radiology, 14(3), 417–424. https://doi.org/10.1007/s00330-003-2220-1

Hartung, G., Pfannmoeller, J., Berman, A., & Polimeni, J. (n.d.). Simulated fMRI responses using human Vascular Anatomical Network models with varying architecture and dynamics. 0682. https://doi.org/10.58530/2022/0682

Harrigan M.R. and Deveikis J.P. (2009) Handbook of Cerebrovascular Disease and Neurointerventional Technique. *AJNR: American Journal of Neuroradiology*, *30*(9), E135. https://doi.org/10.3174/ajnr.A1708

Hassouna, M. S., Farag, A. A., Hushek, S., & Moriarty, T. (2006). Cerebrovascular segmentation from TOF using stochastic models. Medical Image Analysis, 10(1), 2–18. https://doi.org/10.1016/j.media.2004.11.009

Herman, L. H., Fernando, O. U., & Gurdjian, E. S. (1966a). The anterior choroidal artery: An anatomical study of its area of distribution. The Anatomical Record, 154(1), 95–101. https://doi.org/10.1002/ar.1091540109

Herman, L. H., Fernando, O. U., & Gurdjian, E. S. (1966b). The anterior choroidal artery: An anatomical study of its area of distribution. The Anatomical Record, 154(1), Article 1. https://doi.org/10.1002/ar.1091540109

Heverhagen, J. T., Bourekas, E., Sammet, S., Knopp, M. V., & Schmalbrock, P. (2008). Time-of-Flight Magnetic Resonance Angiography at 7 Tesla: Investigative Radiology, 43(8), 568–573. https://doi.org/10.1097/RLI.0b013e31817e9b2c

Huber, L., Ivanov, D., Handwerker, D. A., Marrett, S., Guidi, M., Uludağ, K., Bandettini, P. A., & Poser, B. A. (2018). Techniques for blood volume fMRI with VASO: From low-resolution mapping towards sub-millimeter layer-dependent applications. NeuroImage, 164, 131–143. https://doi.org/10.1016/j.neuroimage.2016.11.039

Huck, J., Wanner, Y., Fan, A. P., Jäger, A.-T., Grahl, S., Schneider, U., Villringer, A., Steele, C. J., Tardif, C. L., Bazin, P.-L., & Gauthier, C. J. (2019). High resolution atlas of the venous brain vasculature from 7 T quantitative susceptibility maps. Brain Structure and Function, 224(7), 2467–2485. https://doi.org/10.1007/s00429-019-01919-4

Hussein, S., Renella, R. R., & Dietz, H. (1988). Microsurgical anatomy of the anterior choroidal artery. Acta Neurochirurgica, 92(1–4), 19–28. https://doi.org/10.1007/BF01401968

Jann, K., Gee, D. G., Kilroy, E., Schwab, S., Smith, R. X., Cannon, T. D., & Wang, D. J. J. (2015). Functional connectivity in BOLD and CBF data: Similarity and reliability of resting brain networks. NeuroImage, 106, 111–122. https://doi.org/10.1016/j.neuroimage.2014.11.028

Kang, C.-K., Kim, S.-H., Lee, H., Park, C.-A., Kim, Y.-B., & Cho, Z.-H. (2010). Functional MR angiography using phase contrast imaging technique at 3T MRI. *NeuroImage*, *50*(3), 1036–1043. https://doi.org/10.1016/j.neuroimage.2010.01.038

Kang, C.-K., Son, Y.-D., & Kim, H.-K. (2016). Energy Spectrum-based Variable-Density Sampling Distribution Optimized for MR Angiography at Compressed Sensing Technique. Applied Magnetic Resonance, 47(2), 201–210. https://doi.org/10.1007/s00723-015-0742-8

Kawamata, T., Takeshita, M., Ishizuka, N., & Hori, T. (2001). Patent Foramen Ovale as a Possible Risk Factor for Cryptogenic Brain Abscess: Report of Two Cases. Neurosurgery, 49(1), 204–207. https://doi.org/10.1097/00006123-200107000-00032

Kim, S. (1995). Quantification of relative cerebral blood flow change by flow-sensitive alternating inversion recovery (FAIR) technique: Application to functional mapping. Magnetic Resonance in Medicine, 34(3), 293–301. https://doi.org/10.1002/mrm.1910340303

Kim, S.-E., & Parker, D. L. (2012). Time-of-Flight Angiography. In J. C. Carr & T. J. Carroll (Eds.), Magnetic Resonance Angiography (pp. 39–50). Springer New York. https://doi.org/10.1007/978-1-4419-1686-0_2

Koopmans, P. J., Manniesing, R., Niessen, W. J., Viergever, M. A., & Barth, M. (2008). MR venography of the human brain using susceptibility weighted imaging at very high field strength. Magnetic Resonance Materials in Physics, Biology and Medicine, 21(1–2), 149–158. https://doi.org/10.1007/s10334-007-0101-3

Korosec, F. R. (2012). Basic Principles of MRI and MR Angiography. In J. C. Carr & T. J. Carroll (Eds.), Magnetic Resonance Angiography (pp. 3–38). Springer New York. https://doi.org/10.1007/978-1-4419-1686-0_1

Kuo, A. H., Nagpal, P., Ghoshhajra, B. B., & Hedgire, S. S. (2019). Vascular magnetic resonance angiography techniques. Cardiovascular Diagnosis and Therapy, 9(S1), S28–S36. https://doi.org/10.21037/cdt.2019.06.07

Kwan, B. Y. M., Salehi, F., Ohorodnyk, P., Lee, D. H., Burneo, J. G., Mirsattari, S. M., Steven, D., Hammond, R., Peters, T. M., & Khan, A. R. (2016). Usage of SWI (susceptibility weighted imaging) acquired at 7 T for qualitative evaluation of temporal lobe epilepsy patients with histopathological and clinical correlation: An initial pilot study. Journal of the Neurological Sciences, 369, 82–87. https://doi.org/10.1016/j.jns.2016.07.066

Kwong, K. K., Chesler, D. A., Weisskoff, R. M., Donahue, K. M., Davis, T. L., Ostergaard, L., Campbell, T. A., & Rosen, B. R. (1995). Mr perfusion studies with t 1 -weighted echo planar imaging. Magnetic Resonance in Medicine, 34(6), 878–887. https://doi.org/10.1002/mrm.1910340613

Langkammer, C., Schweser, F., Krebs, N., Deistung, A., Goessler, W., Scheurer, E., Sommer, K., Reishofer, G., Yen, K., Fazekas, F., Ropele, S., & Reichenbach, J. R. (2012). Quantitative susceptibility mapping (QSM) as a means to measure brain iron? A post mortem validation study. NeuroImage, 62(3), 1593–1599. https://doi.org/10.1016/j.neuroimage.2012.05.049

Larkman, D. J., & Nunes, R. G. (2007). Parallel magnetic resonance imaging. Physics in Medicine and Biology, 52(7), R15–R55. https://doi.org/10.1088/0031-9155/52/7/R01

Larson, T. C., Kelly, W. M., Ehman, R. L., & Wehrli, F. W. (1990). Spatial misregistration of vascular flow during MR imaging of the CNS: Cause and clinical significance. American Journal of Roentgenology, 155(5), 1117–1124. https://doi.org/10.2214/ajr.155.5.2120946

Lee, Y.-B., Seo, Y.-B., Park, C.-A., & Kang, C.-K. (2015). Imaging method for changes in venous dynamics: A preliminary study. NeuroReport, 26(6), 333–340. https://doi.org/10.1097/WNR.0000000000000349

Lesage, D., Angelini, E. D., Bloch, I., & Funka-Lea, G. (2009). A review of 3D vessel lumen segmentation techniques: Models, features and extraction schemes. Medical Image Analysis, 13(6), 819–845. https://doi.org/10.1016/j.media.2009.07.011

Lipton. (2014, September 23). *Introducing MRI: Time of flight effects and MRA (43 of 56)*. YouTube. https://youtu.be/kBrLUaEJaLU

Liu, J., Chen, F., Wang, X., Zhang, X., Sun, K., Xue, R., & Liao, H. (2021). A comparative analysis framework of 3T and 7T TOF-MRA based on automated cerebrovascular segmentation. Computerized Medical Imaging and Graphics, 89, 101830. https://doi.org/10.1016/j.compmedimag.2020.101830

Liu, S., Mok, K., Neelavalli, J., Cheng, Y.-C. N., Tang, J., Ye, Y., & Haacke, E. M. (2014). Improved MR venography using quantitative susceptibility-weighted imaging: True Susceptibility-Weighted Imaging. Journal of Magnetic Resonance Imaging, 40(3), 698–708. https://doi.org/10.1002/jmri.24413

Logothetis, N. K. (2002). The neural basis of the blood–oxygen–level–dependent functional magnetic resonance imaging signal. Philosophical Transactions of the Royal Society of London. Series B: Biological Sciences, 357(1424), 1003–1037. https://doi.org/10.1098/rstb.2002.1114

Logothetis, N. K. (2008). What we can do and what we cannot do with fMRI. Nature, 453(7197), 869–878. https://doi.org/10.1038/nature06976

Logothetis, N. K., & Wandell, B. A. (2004). Interpreting the BOLD Signal. Annual Review of Physiology, 66(1), 735–769. https://doi.org/10.1146/annurev.physiol.66.082602.092845

Lu, H., Golay, X., Pekar, J. J., & Van Zijl, P. C. M. (2003a). Functional magnetic resonance imaging based on changes in vascular space occupancy. Magnetic Resonance in Medicine, 50(2), 263–274. https://doi.org/10.1002/mrm.10519

Lu, H., Golay, X., Pekar, J. J., & Van Zijl, P. C. M. (2003b). Functional magnetic resonance imaging based on changes in vascular space occupancy. Magnetic Resonance in Medicine, 50(2), 263–274. https://doi.org/10.1002/mrm.10519

Lu, H., & Van Zijl, P. C. M. (2012). A review of the development of Vascular-Space-Occupancy (VASO) fMRI. NeuroImage, 62(2), 736–742. https://doi.org/10.1016/j.neuroimage.2012.01.013

Maderwald, S., Ladd, S. C., Gizewski, E. R., Kraff, O., Theysohn, J. M., Wicklow, K., Moenninghoff, C., Wanke, I., Ladd, M. E., & Quick, H. H. (2008). To TOF or not to TOF: Strategies for non-contrast-enhanced intracranial MRA at 7 T. Magnetic Resonance Materials in Physics, Biology and Medicine, 21(1–2), 159–167. https://doi.org/10.1007/s10334-007-0096-9

Manbachi, A., Hoi, Y., Wasserman, B. A., Lakatta, E. G., & Steinman, D. A. (2011). On the shape of the common carotid artery with implications for blood velocity profiles. Physiological Measurement, 32(12), 1885–1897. https://doi.org/10.1088/0967-3334/32/12/001

Medcalf, J. E., Paul Johnson, C., Taktak, A., & Grabherr, S. (2016). Variations in the anatomy of the vertebral artery cervical loop segment—A potential predisposing factor for traumatic basal subarachnoid hemorrhage? Forensic Science, Medicine, and Pathology, 12(4), 444–450. https://doi.org/10.1007/s12024-016-9819-4

Mende, K. A., Froehlich, J. M., Von Weymarn, C., Hoogeveen, R., Kistler, T., Zollikofer, C. L., & Wentz, K. U. (2007). Time-resolved, high-resolution contrast-enhanced MR angiography of dialysis shunts using the CENTRA keyhole technique with parallel imaging. Journal of Magnetic Resonance Imaging, 25(4), 832–840. https://doi.org/10.1002/jmri.20879

Menon, R. S., Ogawa, S., Tank, D. W., & Uğurbil, K. (1993). 4 Tesla gradient recalled echo characteristics of photic stimulation-induced signal changes in the human primary visual cortex. Magnetic Resonance in Medicine, 30(3), 380–386. https://doi.org/10.1002/mrm.1910300317

Nägele, T., Klose, U., Grodd, W., Voigt, K., & Nüsslin, F. (1995). Nonlinear excitation profiles for three-dimensional inflow MR angiography. Journal of Magnetic Resonance Imaging, 5(4), 416–420. https://doi.org/10.1002/jmri.1880050408

Nair, D. G. (2005). About being BOLD. Brain Research Reviews, 50(2), 229–243. https://doi.org/10.1016/j.brainresrev.2005.07.001

Ogawa, S., Lee, T. M., Kay, A. R., & Tank, D. W. (1990). Brain magnetic resonance imaging with contrast dependent on blood oxygenation. Proceedings of the National Academy of Sciences, 87(24), 9868–9872. https://doi.org/10.1073/pnas.87.24.9868

Ogawa, S., Menon, R. S., Tank, D. W., Kim, S. G., Merkle, H., Ellermann, J. M., & Ugurbil, K. (1993). Functional brain mapping by blood oxygenation level-dependent contrast magnetic resonance imaging. A comparison of signal characteristics with a biophysical model. Biophysical Journal, 64(3), 803–812. https://doi.org/10.1016/S0006-3495(93)81441-3

Palomeras, E., Fossas, P., Cano, A. T., Sanz, P., & Floriach, M. (2008). Anterior choroidal artery infarction: A clinical, etiologic and prognostic study. Acta Neurologica Scandinavica, 118(1), 42–47. https://doi.org/10.1111/j.1600-0404.2007.00980.x

Park, C.-A., Kang, C.-K., Kim, Y.-B., & Cho, Z.-H. (2015). Examining the resting-state vascular connectivity using fMRA in comparison with fMRI: A preliminary study. NeuroReport, 26(11), 623–628. https://doi.org/10.1097/WNR.0000000000000399

Park, C.-A., Kang, C.-K., Kim, Y.-B., & Cho, Z.-H. (2018). Advances in MR angiography with 7T MRI: From microvascular imaging to functional angiography. NeuroImage, 168, 269–278. https://doi.org/10.1016/j.neuroimage.2017.01.019

Parker, D. L., Yuan, C., & Blatter, D. D. (1991). MR angiography by multiple thin slab 3D acquisition. Magnetic Resonance in Medicine, 17(2), 434–451. https://doi.org/10.1002/mrm.1910170215

Pflugfelder, D., Vahedipour, K., Uludağ, K., Shah, N. J., & Stöcker, T. (2011). On the numerically predicted spatial BOLD fMRI specificity for spin echo sequences. Magnetic Resonance Imaging, 29(9), 1195–1204. https://doi.org/10.1016/j.mri.2011.07.015

Rapacchi, S., Natsuaki, Y., Plotnik, A., Gabriel, S., Laub, G., Finn, J. P., & Hu, P. (2015). Reducing view-sharing using compressed sensing in time-resolved contrast-enhanced magnetic resonance angiography. Magnetic Resonance in Medicine, 74(2), 474–481. https://doi.org/10.1002/mrm.25414

Reichenbach, J. R., Essig, M., Haacke, E. M., Lee, B. C., Przetak, C., Kaiser, W. A., & Schad, L. R. (1998). High-resolution venography of the brain using magnetic resonance imaging. Magnetic Resonance Materials in Physics, Biology and Medicine, 6(1), 62–69. https://doi.org/10.1007/BF02662513

Reichenbach, J. R., Jonetz-Mentzel, L., Fitzek, C., Haacke, E. M., Kido, D. K., Lee, B. C. P., & Kaiser, W. A. (2001). High-resolution blood oxygen-level dependent MR venography (HRBV): A new technique. Neuroradiology, 43(5), 364–369. https://doi.org/10.1007/s002340000503

Rhoton, A. L., Jr, Fujii, K., & Fradd, B. (1979). Microsurgical anatomy of the anterior choroidal artery. Surgical neurology, 12(2), 171–187.

Rui Gan, Chung, A. C. S., Wong, W. C. K., & Yu, S. C. H. (2004). Vascular segmentation in three-dimensional rotational angiography based on maximum intensity projections. 2004 2nd IEEE International Symposium on Biomedical Imaging: Macro to Nano (IEEE Cat No. 04EX821), 2, 133–136. https://doi.org/10.1109/ISBI.2004.1398492

Saleh, M. D., Eswaran, C., & Mueen, A. (2011). An Automated Blood Vessel Segmentation Algorithm Using Histogram Equalization and Automatic Threshold Selection. Journal of Digital Imaging, 24(4), 564–572. https://doi.org/10.1007/s10278-010-9302-9

Schaller, B. (2004). Physiology of cerebral venous blood flow: From experimental data in animals to normal function in humans. Brain Research Reviews, 46(3), 243–260. https://doi.org/10.1016/j.brainresrev.2004.04.005

Schmitter, S., Bock, M., Johst, S., Auerbach, E. J., Uğurbil, K., & Van de Moortele, P. (2011). Contrast enhancement in TOF cerebral angiography at 7 T using saturation and MT pulses under SAR constraints: Impact of verse and sparse pulses. *Magnetic Resonance in Medicine*, *68*(1), 188–197. https://doi.org/10.1002/mrm.23226

Schrauben, E. M., Johnson, K. M., Huston, J., Del Rio, A. M., Reeder, S. B., Field, A., & Wieben, O. (2014). Reproducibility of Cerebrospinal Venous Blood Flow and Vessel Anatomy with the Use of Phase Contrast-Vastly Undersampled Isotropic Projection Reconstruction and Contrast-Enhanced MRA. American Journal of Neuroradiology, 35(5), 999–1006. https://doi.org/10.3174/ajnr.A3779

Scouten, A., & Constable, R. T. (2007). Applications and limitations of whole-brain MAGIC VASO functional imaging. Magnetic Resonance in Medicine, 58(2), 306–315. https://doi.org/10.1002/mrm.21273

Serres , B., Deistung, A., Schfer , A., Kocinski , M., Materka , A., & Reichenbach , J. (2015). Automatic segmentation of the venous vessel network based on quantitative susceptibility maps and its application to investigate blood oxygenation. (ISMRM 2015) Automatic Segmentation of the Venous Vessel Network Based on Quantitative Susceptibility Maps and its Application to Investigate Blood Oxygenation. https://archive.ismrm.org/2015/0169.html

Shao, X., Yan, L., Ma, S. J., Wang, K., & Wang, D. J. J. (2021). High-Resolution Neurovascular Imaging at 7T. Magnetic Resonance Imaging Clinics of North America, 29(1), 53–65. https://doi.org/10.1016/j.mric.2020.09.003

Shi, Z., Zhao, X., Zhu, S., Miao, X., Zhang, Y., Han, S., Wang, B., Zhang, B., Ye, X., Dai, Y., Chen, C., Rao, S., Lin, J., Zeng, M., & Wang, H. (2023). Time-of-Flight Intracranial MRA at 3 T versus 5 T versus 7 T: Visualization of Distal Small Cerebral Arteries. Radiology, 306(1), 207–217. https://doi.org/10.1148/radiol.220114

Solberg, L. A., & Eggen, D. A. (1971). Localization and Sequence of Development of Atherosclerotic Lesions in the Carotid and Vertebral Arteries. Circulation, 43(5), 711–724. https://doi.org/10.1161/01.CIR.43.5.711

Standring, S., Ellis, H., Healy, J., Johnson, D., Williams, A., Collins, P., & Wigley, C. (2005). Gray's anatomy: the anatomical basis of clinical practice. *American journal of neuroradiology*, *26*(10), 2703.

Standring, S. (2015). *Gray's Anatomy E-Book: The Anatomical Basis of Clinical Practice*. Elsevier Health Sciences

Stefani, M. A., Schneider, F. L., Marrone, A. C. H., Severino, A. G., Jackowski, A. P., & Wallace, M. C. (2000). Anatomic variations of anterior cerebral artery cortical branches. Clinical Anatomy, 13(4), 231–236. https://doi.org/10.1002/1098-2353(2000)13:4<231::AID-CA1>3.0.CO;2-T

Stüber, C., Morawski, M., Schäfer, A., Labadie, C., Wähnert, M., Leuze, C., Streicher, M., Barapatre, N., Reimann, K., Geyer, S., Spemann, D., & Turner, R. (2014). Myelin and iron concentration in the human brain: A quantitative study of MRI contrast. NeuroImage, 93, 95–106. https://doi.org/10.1016/j.neuroimage.2014.02.026

Tatu, L., Moulin, T., Bogousslavsky, J., & Duvernoy, H. (1998). Arterial territories of the human brain: Cerebral hemispheres. Neurology, 50(6), 1699–1708. https://doi.org/10.1212/WNL.50.6.1699

Tatu, L., Vuillier, F., & Moulin, T. (2009). Chapter 13 Anatomy of the circulation of the brain and spinal cord. In Handbook of Clinical Neurology (Vol. 92, pp. 247–281). Elsevier. https://doi.org/10.1016/S0072-9752(08)01913-1

Turk, A. S., Johnson, K. M., Lum, D., Niemann, D., Aagaard-Kienitz, B., Consigny, D., Grinde, J., Turski, P., Haughton, V., & Mistretta, C. (2007). Physiologic and anatomic assessment of a canine carotid artery stenosis model utilizing phase contrast with vastly undersampled isotropic projection imaging. AJNR. American Journal of Neuroradiology, 28(1), 111–115.

Uludağ, K., & Blinder, P. (2018). Linking brain vascular physiology to hemodynamic response in ultra-high field MRI. NeuroImage, 168, 279–295. https://doi.org/10.1016/j.neuroimage.2017.02.063

Uludağ, K., Müller-Bierl, B., & Uğurbil, K. (2009). An integrative model for neuronal activity-induced signal changes for gradient and spin echo functional imaging. NeuroImage, 48(1), 150–165. https://doi.org/10.1016/j.neuroimage.2009.05.051

Villringer, A., & Einhäupl, K. M. (1997). Dural sinus and cerebral venous thrombosis. *New horizons (Baltimore, Md.)*, *5*(4), 332–341.

Von Morze, C., Xu, D., Purcell, D. D., Hess, C. P., Mukherjee, P., Saloner, D., Kelley, D. A. C., & Vigneron, D. B. (2007). Intracranial time-of-flight MR angiography at 7T with comparison to 3T. Journal of Magnetic Resonance Imaging, 26(4), 900–904. https://doi.org/10.1002/jmri.21097

Wang, Y., & Liu, T. (2015). Quantitative susceptibility mapping (QSM): Decoding MRI data for a tissue magnetic biomarker. Magnetic Resonance in Medicine, 73(1), 82–101. https://doi.org/10.1002/mrm.25358

Wen, L., Wang, X., Wu, Z., Zhou, M., & Jin, J. S. (2015). A novel statistical cerebrovascular segmentation algorithm with particle swarm optimization. Neurocomputing, 148, 569–577. https://doi.org/10.1016/j.neucom.2014.07.006

Wu, C. W., Chuang, K., Wai, Y., Wan, Y., Chen, J., & Liu, H. (2008). Vascular space occupancy-dependent functional MRI by tissue suppression. Journal of Magnetic Resonance Imaging, 28(1), 219–226. https://doi.org/10.1002/jmri.21410

Wu, E. X., Hui, E. S., & Cheung, J. S. (2007). TOF-MRA using multi-oblique-stack acquisition (MOSA). Journal of Magnetic Resonance Imaging, 26(2), 432–436. https://doi.org/10.1002/jmri.20954

Xiao, R., Ding, H., Zhai, F., Zhou, W., & Wang, G. (2018). Cerebrovascular segmentation of TOF-MRA based on seed point detection and multiple-feature fusion. Computerized Medical Imaging and Graphics, 69, 1–8. https://doi.org/10.1016/j.compmedimag.2018.07.002

Yasuda, A., Campero, A., Martins, C., Rhoton, A. L., De Oliveira, E., & Ribas, G. C. (2008). MICROSURGICAL ANATOMY AND APPROACHES TO THE CAVERNOUS SINUS. Neurosurgery, 62(6), SHC1240–SHC1263. https://doi.org/10.1227/01.NEU.0000333790.90972.59

Zarrinkoob, L., Ambarki, K., Wåhlin, A., Birgander, R., Eklund, A., & Malm, J. (2015a). Blood Flow Distribution in Cerebral Arteries. Journal of Cerebral Blood Flow & Metabolism, 35(4), 648–654. https://doi.org/10.1038/jcbfm.2014.241

Zarrinkoob, L., Ambarki, K., Wåhlin, A., Birgander, R., Eklund, A., & Malm, J. (2015b). Blood Flow Distribution in Cerebral Arteries. Journal of Cerebral Blood Flow & Metabolism, 35(4), Article 4. https://doi.org/10.1038/jcbfm.2014.241

Zhao, F., Chen, Y., Hou, Y., & He, X. (2017). Segmentation of blood vessels using rule-based and machine-learning-based methods: A review. Multimedia Systems, 25(2), 109–118. https://doi.org/10.1007/s00530-017-0580-7